iScience

CellPress
OPEN ACCESS

Review

Recent advances in design of lanthanide-containing NIR-II luminescent nanoprobes

Yingjie Yang,[1,2] Datao Tu,[1,3,*] Yunqin Zhang,[1,2] Peng Zhang,[1] and Xueyuan Chen[1,2,3,*]

SUMMARY

Luminescent biosensing in the second near-infrared window (NIR-II, 1000–1700 nm) region, which has weak tissue scattering and low autofluorescence, draws extensive attention owing to its deep tissue penetration, good spatial resolution and high signal-to-background ratio. As a new generation of NIR-II probes, lanthanide (Ln^{3+})-containing nanoprobes exhibit several superior properties. With the rapid development of Ln^{3+}-containing NIR-II nanoprobes, many significant advances have been accomplished in their optical properties tuning and surface functional modification for further bioapplications. Rather than being exhaustive, this review aims to survey the recent advances in the design strategies of inorganic Ln^{3+}-containing NIR-II luminescent nanoprobes by highlighting their optical performance optimization and surface modification approaches. Moreover, challenges and opportunities for this kind of novel NIR-II nanoprobes are envisioned.

INTRODUCTION

In the second near-infrared (NIR-II, 1000–1700 nm) window, the effects of scattering and autofluorescence that come from endogenous fluorophores in tissues are minimized with the increasing wavelengths (Fan and Zhang, 2019; He et al., 2019; Li et al., 2020c; Naczynski et al., 2013; Wang et al., 2019). Compared with NIR-I imaging, NIR-II imaging can afford higher resolution with deeper penetration depth and lower background noise in biological tissues, which shows more potential for clinical translation (Diao et al., 2015; Kong et al., 2016; Wang et al., 2018d; Hu et al., 2020a, 2020b). With the development of noninvasive NIR-II imaging technique, the exploitation of efficient NIR-II luminescent probes has become an urgent task (He et al., 2018; Zhong and Dai, 2020). So far, the most developed NIR-II probes mainly fall into five categories: single-walled carbon nanotubes (SWCNTs) (Kodach et al., 2010; Welsher et al., 2009), quantum dots (QDs) (Dong et al., 2013; Xu et al., 2016), conjugated polymers (Hong et al., 2014; Reineck and Gibson, 2017), organic dyes (Antaris et al., 2016; Semonin et al., 2010; Thimsen et al., 2017), and lanthanide (Ln^{3+})-containing probes (Dai et al., 2017; Stouwdam and van Veggel, 2002; Xu et al., 2019; Heffern et al., 2014; Peng et al., 2020; Ning et al., 2019; Jin et al., 2020; Hu et al., 2017). Among them, SWCNTs usually exhibit broadband emission (>300 nm) and low photoluminescence (PL) quantum yields (QYs) (0.1–0.4%). QDs mostly face the problem of high toxicity (Wang and Zhang, 2014). As for conjugated polymers and organic dyes, they both display low solubility in aqueous solutions and suffer from photobleaching (Escobedo et al., 2010; Shen et al., 2020). All these drawbacks limit their practical bioapplications. In comparison with the aforementioned NIR-II probes, Ln^{3+}-containing NIR-II luminescent nanoprobes are particularly intriguing because of their unique electronic structures and optical properties. Ln^{3+} ions have the electron configuration of $4f^n5s^25p^6$ (n = 0–14). Specifically, the rich energy levels of Ln^{3+} endow their emissions covering from UV, visible to NIR. Among Ln^{3+} ions, several ions like Yb^{3+}, Tm^{3+}, Er^{3+}, Ho^{3+}, Dy^{3+}, Sm^{3+}, Nd^{3+}, and Pr^{3+} were reported to produce NIR-II light (Naczynski et al., 2013; Yu et al., 2019). The inner 4f-4f transitions of these Ln^{3+} are insensitive to outer environment due to the effective shielding of 4f orbitals by the filled 5s and 5p orbitals, which results in sharp and tunable emissions with high photostability. As a new generation of NIR-II probes, Ln^{3+}-containing nanoparticles (NPs) show great potential for multiplexed sensing, time-gated detection, and high-resolution imaging (Naczynski et al., 2014; Tan et al., 2020; Yu et al., 2008; Zhang et al., 2015; Wang et al., 2017a; Huang et al., 2015).

To date, significant efforts have been made to design highly efficient Ln^{3+}-containing NIR-II luminescent nanoprobes (Liu et al., 2011; Swabeck et al., 2018; Xiao et al., 2013; Yu et al., 2008; Zhou et al., 2013). It

[1]CAS Key Laboratory of Design and Assembly of Functional Nanostructures, and Fujian Key Laboratory of Nanomaterials, Fujian Institute of Research on the Structure of Matter, Chinese Academy of Sciences, Fuzhou 350002, China

[2]University of Chinese Academy of Sciences, Beijing 100049, China

[3]Fujian Science & Technology Innovation Laboratory for Optoelectronic Information of China, Fuzhou, Fujian 350108, China

*Correspondence: dttu@fjirsm.ac.cn (D.T.), xchen@fjirsm.ac.cn (X.C.)

https://doi.org/10.1016/j.isci.2021.102062

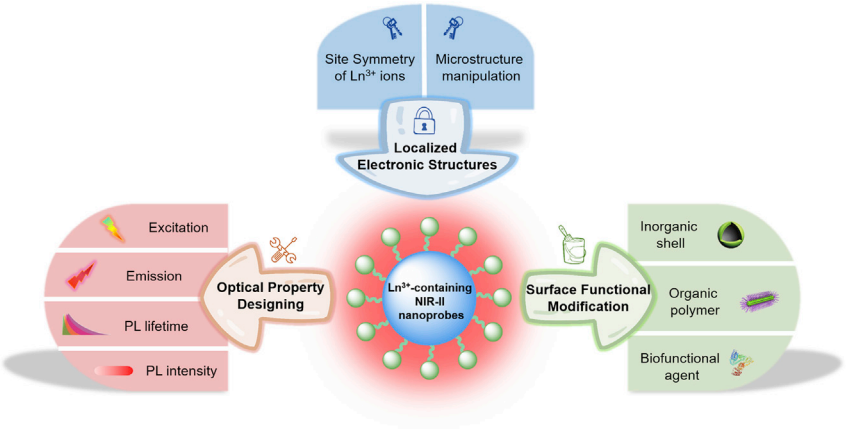

Figure 1. Summary of Ln^{3+}-containing NIR-II luminescent nanoprobes from fundamentals to design strategies

should be noted that most of the recently published reviews mainly emphasized on the chemistry and potential applications of Ln^{3+}-containing NIR-II nanoprobes in bioimaging, biodetection, and disease theranostics (Yu et al., 2020; Li et al., 2020b; Wang and Zhang, 2016). Up to now, few reviews focused on their fundamental electronic structures and optical design, which should be renewed since more progress or new understandings have been gained in the past few years. Therefore, in this review, we provide a comprehensive survey of the latest advances toward the design of inorganic Ln^{3+}-containing NIR-II nanoprobes, which covers from their fundamental electronic structures to novel design strategies, highlighting the optical performance optimization and surface modification approaches. This review will be organized as shown in Figure 1. Firstly, we start by the localized electronic structures of Ln^{3+}-containing NIR-II nanoprobes. Then, the optical properties tuning of NIR-II nanoprobes will be reviewed, with emphasis on excitation/emission manipulation, PL lifetime manipulation, and PL intensity improvement. Furthermore, a variety of surface modification strategies like inorganic shell coating, organic polymer modification, and biofunctional agent conjugation will be briefly discussed. Finally, emerging trends and further efforts are proposed.

LOCALIZED ELECTRONIC STRUCTURES

Inorganic Ln^{3+}-containing NPs are typically composed of Ln^{3+} emitters and a suitable inorganic host, which possesses good photo-chemical stability and high optical damage threshold. The intricate optical properties of trivalent Ln^{3+} originate from their $4f^n$ inner shell configurations, which have very localized states and can be conventionally described with crystal-field (CF) theory. Located in a dielectric crystal, the energy levels of Ln^{3+} ions split under the influence of the electric field produced by the crystalline environment. A small difference of the localized electronic structures may result in significant change in the electronic energy levels and excited-state dynamics of the doped Ln^{3+} ions. In this section, the site symmetry of Ln^{3+} ions and the microstructure manipulation of Ln^{3+}-containing NIR-II nanoprobes are surveyed, which are essentially important to design novel Ln^{3+}-containing NIR-II luminescent nanoprobes.

Site symmetry of lanthanide ions

The optical properties of Ln^{3+} strongly depend on the local site symmetry and CF surroundings around Ln^{3+}. The inorganic NPs generally suffer from structure distortion and surface defects after the introduction of Ln^{3+} ions into their lattices, which may lead to the multiple sites of Ln^{3+} with diverse CF surroundings. Accordingly, the site symmetries of Ln^{3+} ions in the inorganic NPs can be verified by means of high-resolution site-selective or time-resolved PL spectroscopy.

As a typical example, our group employed Eu^{3+} as a spectroscopic probe to unveil the local site symmetry of NIR-II $LiLuF_4$:Nd^{3+} NPs through high-resolution PL spectroscopy (Huang et al., 2019). The detailed assignment of the CF transition lines of Eu^{3+} was achieved through 10 K PL spectra of $LiLuF_4$:5 mol% Eu^{3+} NPs to avoid thermal broadening of spectral lines at room temperature. As a result, total numbers of 0, 2, 3, 4, and 4 CF transition lines of Eu^{3+} from $^5D_0$ to $^7F_0$, $^7F_1$, $^7F_2$, $^7F_3$, and $^7F_4$ can be discerned in $LiLuF_4$

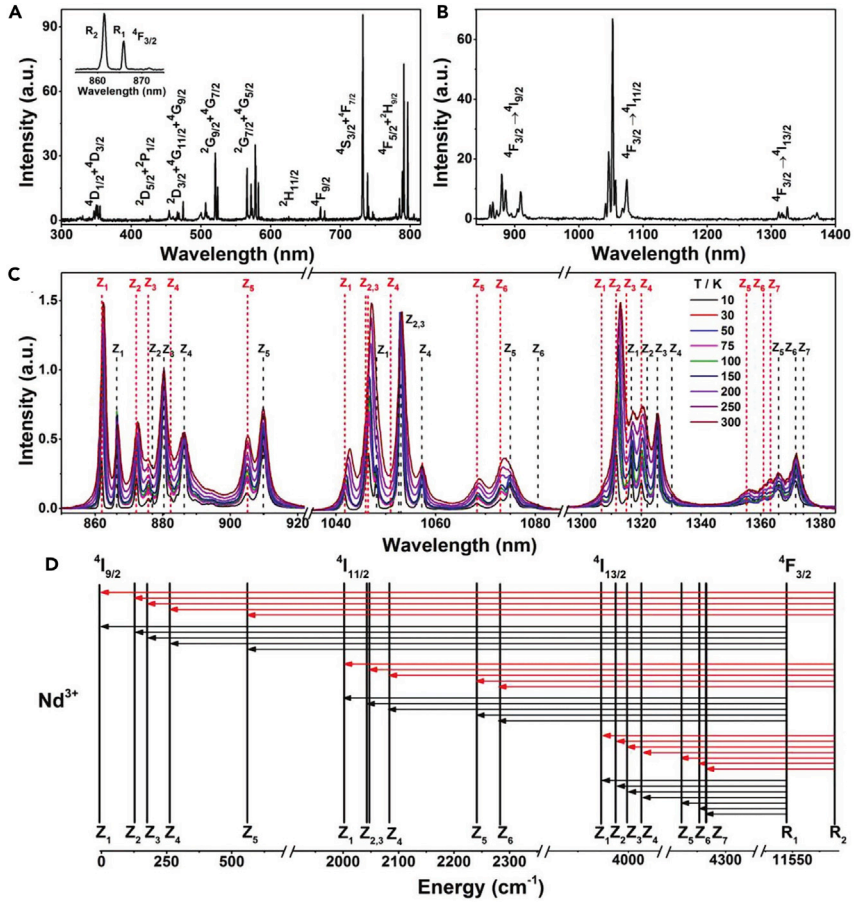

Figure 2. Assignment of the CF transition lines of Nd^{3+} in $LiLuF_4$ NPs through high-resolution PL spectroscopy

(A) 10 K PL excitation spectrum of $LiLuF_4$:2 mol%Nd^{3+} NPs by monitoring the Nd^{3+} emission at 1053.2 nm. Inset shows two CF transition lines from the $^4I_{9/2}$ ground state to the upper and lower Stark sublevels of $^4F_{3/2}$.

(B) 10 K PL emission spectrum of $LiLuF_4$:2 mol%Nd^{3+} NPs upon excitation at 791.3 nm.

(C) Temperature-dependent PL emission spectra (10–300 K) for the $^4F_{3/2} \rightarrow {}^4I_J$ (J = 9/2, 11/2, and 13/2) CF transitions of Nd^{3+} in $LiLuF_4$ NPs upon 808-nm diode laser excitation at a power density of 1 W cm^{-2}. The spectra were normalized at the maximum intensities at 880.4, 1053.1, and 1325.1 nm for the emissions from $^4F_{3/2}$ to $^4I_{9/2}$, $^4I_{11/2}$, and $^4I_{13/2}$, respectively. The dash lines denote the CF transitions from the R_1 (black) and R_2 (red) Stark sublevels of $^4F_{3/2}$ to those of ^4I_J.

(D) CF energy levels of the $^4F_{3/2}$ and ^4I_J multiplets of Nd^{3+} in $LiLuF_4$ NPs, showing all CF transitions observed in (C).

Reproduced with permission from Huang et al. (Huang et al., 2019). Copyright 2019, Wiley-VCH.

NPs. Subsequently, the Eu^{3+} ions were verified to occupy a single spectroscopic site through site-selective excitation and emission spectra. According to the branching rules and the transition selection rules of the 32 point groups, the spectroscopic site symmetry of Eu^{3+} in $LiLuF_4$ NPs was determined to be S_4, which agreed well with the crystallographic site symmetry of Lu^{3+} in $LiLuF_4$. In view of the close ionic radii and chemical properties of Ln^{3+} ions, it is suggested that Nd^{3+} ions are prone to occupy a single spectroscopic site of S_4 symmetry in $LiLuF_4$ NPs at low doping levels (<5 mol%). Furthermore, a total number of 36 CF transition lines of Nd^{3+} in the NIR region and the corresponding CF levels were unequivocally assigned with the help of temperature-dependent PL spectroscopy (Figure 2). By monitoring the Nd^{3+} emission at 1053.2 nm, the excitation peaks at 861.4 and 865.9 nm were clearly observed in the PL excitation spectrum of Nd^{3+} in $LiLuF_4$ NPs, which were ascribed to the CF transitions of Nd^{3+} from the $^4I_{9/2}$ ground state to the upper (R_2) and lower (R_1) Stark sublevels of $^4F_{3/2}$, respectively. This implies that the CF levels of Nd^{3+} are doubly degenerate in $LiLuF_4$ NPs. Upon selective excitation with 808-nm diode laser and 791.3-nm xenon lamp, respectively, the identical emission patterns unambiguously confirmed that Nd^{3+} ions in the $LiLuF_4$ NPs occupied a single spectroscopic site. The total numbers of 10, 12, and 14 CF transition lines of Nd^{3+} from $^4F_{3/2}$ to $^4I_{9/2}$, $^4I_{11/2}$, and $^4I_{13/2}$ agreed well with the theoretically predicted numbers for Nd^{3+} in $LiLuF_4$

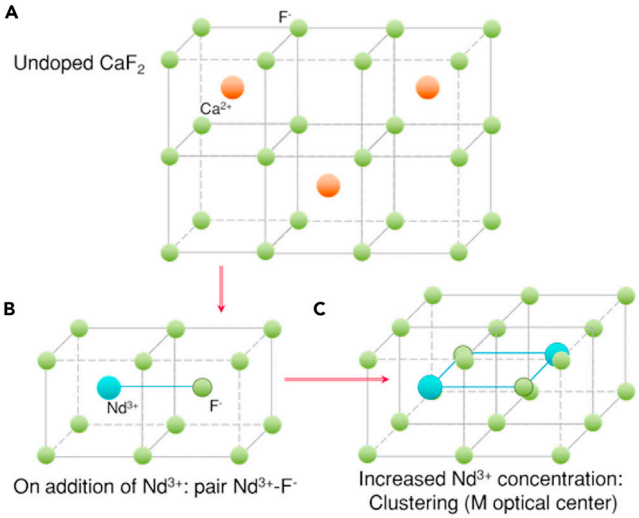

Figure 3. Scheme of the cubic lattice of CaF_2 and the formation of Nd^{3+}-F^- clusters

(A) Scheme of the cubic lattice of CaF_2.

(B) Scheme of the doping of Nd^{3+} in CaF_2. When Nd^{3+} ions are doped to substitute Ca^{2+} ions, fluorine ions are required at the interstitial position to form Nd^{3+}-F^- pair.

(C) Scheme of the CaF_2:Nd^{3+} with high doping content. Upon increasing Nd^{3+} concentration, clusters of Nd^{3+}-F^- pairs are formed.

Reproduced with permission from Quintanilla et al. (Quintanilla et al., 2018). Copyright 2018, American Chemical Society.

with doubly degenerate CF levels. Based on the well-resolved CF transition lines from the thermally coupled Stark sublevels of $^4F_{3/2}$ of Nd^{3+}, the application of $LiLuF_4$:Nd^{3+} NPs as sensitive NIR-to-NIR luminescent nanoprobes for ratiometric detection of cryogenic temperature was subsequently illustrated.

Microstructure manipulation

As is well known, the selection of host lattice with specific symmetry will strongly influence the optical properties of Ln^{3+} dopants (Tu et al., 2013). Besides, the cation incorporation strategy was also demonstrated to effectively manipulate the microstructure of Ln^{3+}-containing NIR-II luminescent NPs to improve their optical performance.

Typically, Y^{3+} ions were co-doped into CaF_2:Nd^{3+} NPs to regulate the local site symmetry for efficient NIR-II emitting of Nd^{3+} (Yu et al., 2018; Quintanilla et al., 2018). The CaF_2 lattice comprises fluorine atoms at the corners of cubes and an alternate calcium atom. Nd^{3+} ions were incorporated into the lattice to substitute Ca^{2+} ions (Figure 3A). As a result of charge compensation, a F^- at an interstitial site was produced (Figure 3B). Upon increasing Nd^{3+} concentration, Nd^{3+}-F^- emitting pairs were created and may form clustering at even higher concentrations (Figure 3C). The formation of clustering reduced the distance of neighboring Nd^{3+} ions, facilitating the unwanted nonradiative transitions. It was revealed that the clustering occurred at rather low Nd^{3+} concentrations (~1 mol%) in CaF_2. With the addition of Y^{3+} ions into the CaF_2 host, the structures of Nd^{3+}-Nd^{3+} clusters were broken and the nonradiative relaxation paths can be hindered. The NIR-II QY of CaF_2:Nd^{3+}, Y^{3+} NPs was measured to be 9.30%, which was ~3 times higher than that of CaF_2:Nd^{3+} NPs. In a parallel study, transition metal ions like Zn^{2+} ions were incorporated into $NaYbF_4$:Er^{3+}, Ce^{3+}@$NaYF_4$ counterparts to further improve the NIR-II PLQY through the doping-caused distortion of local symmetry around Er^{3+} ions (Zhong et al., 2019).

OPTICAL PROPERTY DESIGNING

Benefiting from the peculiar electronic structures of Ln^{3+}, a variety of inorganic Ln^{3+}-containing NIR-II luminescent nanoprobes have been developed (Table 1). To engineer their optical properties for various bioapplications, many efforts have been devoted through tuning the host-dopant combination, the dopant concentration, and the morphology of particles. In this section, we will highlight the strategies of optical property design for these Ln^{3+}-containing NIR-II nanoprobes.

Table 1. Ln^{3+}-containing NIR-II luminescent nanoprobes based on typical Ln^{3+} activators

Activator	Nanoprobe	Ex/Em wavelength (nm)	Energy level transition	PLQY (%)	Reference
Nd^{3+}	$NaGdF_4$:Yb^{3+}, Nd^{3+}, Tm^{3+}	808/1000	$^4F_{3/2}\rightarrow{}^4I_{11/2}$	11	Tan et al., 2018
	$NaNdF_4$: Mn^{2+}	808/1058, 1320	$^4F_{3/2}\rightarrow{}^4I_{11/2}$ $^4F_{3/2}\rightarrow{}^4I_{13/2}$	10	(Wang et al., 2018c)
	CaF_2: Y^{3+}, Nd^{3+}	808/1058, 1328	$^4F_{3/2}\rightarrow{}^4I_{11/2}$ $^4F_{3/2}\rightarrow{}^4I_{13/2}$	9.3	Lei et al., 2018
	$NaYF_4$:Nd^{3+}@$NaYF_4$	808/1064, 1345	$^4F_{3/2}\rightarrow{}^4I_{11/2}$ $^4F_{3/2}\rightarrow{}^4I_{13/2}$	7.9, 4.1	Li et al., 2019a
	CaS:Ce^{3+}, Nd^{3+}	450/1070	$^4F_{3/2}\rightarrow{}^4I_{11/2}$	7.7	Zhang et al., 2019b
Er^{3+}	CaS:Ce^{3+}, Er^{3+}	450/1540	$^4I_{13/2}\rightarrow{}^4I_{15/2}$	9.3	Zhang et al., 2019b
	$NaYF_4$:Gd^{3+}, Yb^{3+}, Er^{3+}	980/1520	$^4I_{13/2}\rightarrow{}^4I_{15/2}$	0.994	Xue et al., 2018
	$NaCeF_4$:Er^{3+}, Yb^{3+}	980/1530	$^4I_{13/2}\rightarrow{}^4I_{15/2}$	32.8	Lei et al., 2018
	$NaYF_4$:Er^{3+}@ICG	808/1520	$^4I_{13/2}\rightarrow{}^4I_{15/2}$	3.1	Wang et al., 2018a
	$NaErF_4$:Yb^{3+}@$NaLuF_4$	808/1525	$^4I_{13/2}\rightarrow{}^4I_{15/2}$	11	Wang et al., 2018c
Ho^{3+}	$Ba_2In_2O_5$:Yb^{3+}, Ho^{3+}	980/1192	$^5I_6\rightarrow{}^5I_8$	-	Wang et al., 2018e
	$NaErF_4$:Ho^{3+}@$NaYF_4$	1530/1180	$^5I_6\rightarrow{}^5I_8$	-	Liu et al., 2018
	$NaYF_4$:Er^{3+}, Ho^{3+}, Yb^{3+}	1532/1172	$^5I_6\rightarrow{}^5I_8$	-	Cheng et al., 2018
	$NaYF_4$:Yb^{3+}, Ho^{3+}@$NaYF_4$	980/1185	$^5I_6\rightarrow{}^5I_8$	-	Naczynski et al., 2013
Tm^{3+}	$NaYF_4$:Yb^{3+}, Tm^{3+}@$NaYF_4$	980/1475	$^3H_4\rightarrow{}^3F_4$	-	Naczynski et al., 2013
Pr^{3+}	$NaYF_4$:Yb^{3+}, Pr^{3+}@$NaYF_4$	980/1310	$^1G_4\rightarrow{}^3H_5$	-	Naczynski et al., 2013

Excitation manipulation

Currently, the most commonly used excitation wavelength for Ln^{3+}-containing NIR-II nanoprobes is 980 nm, which matches well with the absorption of Yb^{3+} ($^2F_{7/2}\rightarrow{}^2F_{5/2}$) (Zhang et al., 2018; Zheng et al., 2015). Upon excitation with a commercial 980-nm diode laser, Yb^{3+} can absorb and transfer the energy to activators such as Er^{3+}, Tm^{3+}, and Nd^{3+}. However, the narrow band absorption and low absorption coefficient of Yb^{3+} limit their further applications. Additionally, 980-nm laser may cause serious tissue overheating problem owing to the significant absorption by water molecules. These concerns greatly motivate the excitation manipulation of these Ln^{3+}-containing NIR-II nanoprobes, with the aim of overcoming the restrictions of 980-nm excitation.

Generally, NIR-II luminescence of Ln^{3+} ions can be achieved through direct excitation or introducing efficient sensitizers (Cheng et al., 2018; Zhang et al., 2020a). Compared with direct excitation, the sensitizers which have broader absorption bands and larger absorption cross-sections can promote the activators to higher excited states through energy transfer (ET) process and then lead to efficient NIR-II emitting. Therefore, suitable sensitizers including organic dyes, QDs, and Ln^{3+} ions were developed to manipulate the excitation.

As antenna, organic dyes with large absorption cross sections were widely selected to broaden the excitation of Ln^{3+}-containing luminescent NPs. In 2012, Zou et al. (2012) first reported the ET process from the NIR dye IR-806 to $NaYF_4$:Yb^{3+}, Er^{3+} NPs. Benefiting from the dye-sensitized process and increased absorption cross section, the excitation spectral response was expanded to a broad range of 720–1000 nm. Inspired by this work, a series of organic dyes were adopted to sensitize Ln^{3+} NIR luminescence, including indocyanine green (Wang et al., 2018a), MY-1057 (Zhao et al., 2020), and IR-1061 (Hazra et al., 2018).

Besides dye sensitization, QDs were also explored as light harvesting materials. CdSe (Martín-Rodríguez et al., 2013), InP (Klik et al., 2002; Swabeck et al., 2018), and $CsPbX_3$ QDs were reported to sensitize the NIR emissions of Ln^{3+}. Among them, $CsPbX_3$ perovskite QDs have drawn most attention because of their broadband absorption and excellent optical properties. Pan et al. (2017) demonstrated that NIR emission was obtained from Yb^{3+}-doped $CsPbCl_3$ QDs upon the excitation of 365-nm light. The sensitization of $CsPbCl_3$ host with large absorption coefficient endowed Yb^{3+} excitation at a broad ultraviolet component

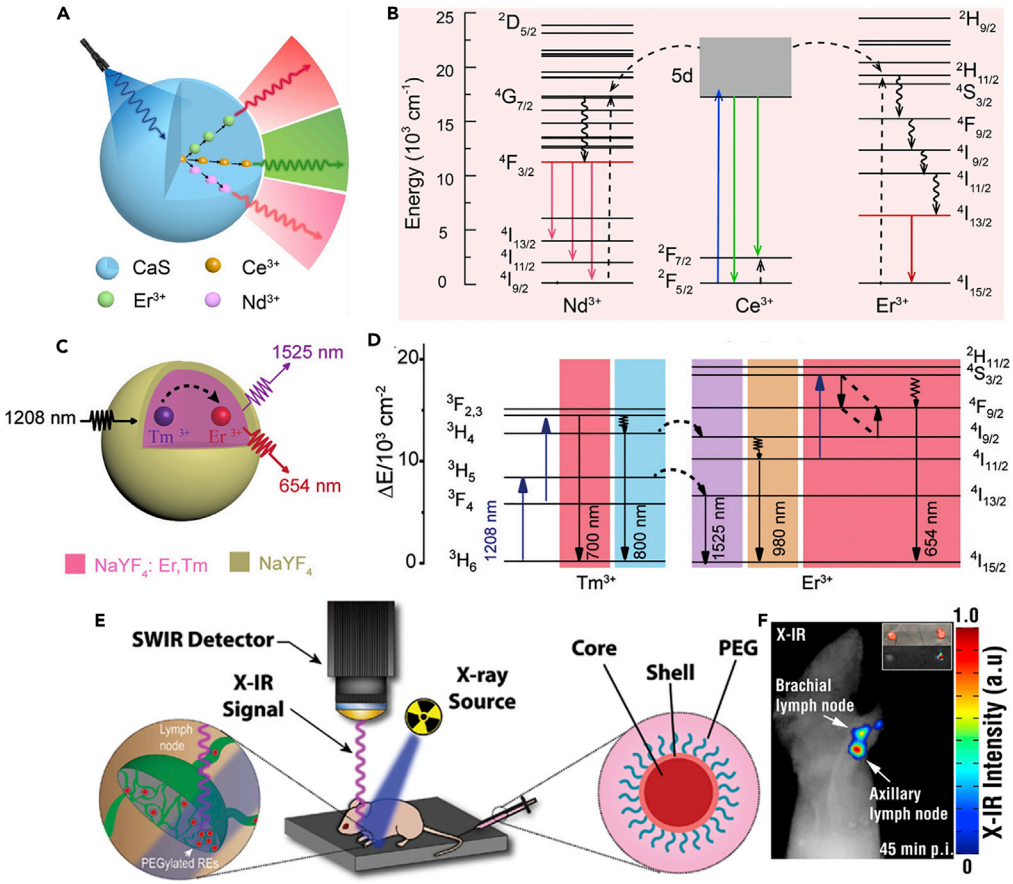

Figure 4. Excitation manipulation of Ln^{3+}-containing NIR-II luminescent nanoprobes

(A) Schematic illustration of the ET from Ce^{3+} to Er^{3+} and Nd^{3+} in CaS NPs.

(B) Simplified energy levels of Ce^{3+}, Er^{3+}, and Nd^{3+} in CaS NPs, showing the proposed ET processes for the population of $^4I_{13/2}$ of Er^{3+} and $^4F_{3/2}$ of Nd^{3+} through sensitization by Ce^{3+}. The dashed, dotted and full arrows represent the ET, nonradiative relaxation and radiative transition processes, respectively.

(C) Schematic design of the as-synthesized $NaYF_4$:Tm^{3+}@$NaYF_4$ and $NaYF_4$:Tm^{3+}, Er^{3+}@$NaYF_4$ NPs excited by a 1208-nm laser (10 W cm^{-2}).

(D) Simplified ET pathway from Tm^{3+} to Er^{3+}.

(E) X-IR system used to image Ln^{3+}-doped NPs consists of a highly sensitive NIR-II detector and X-ray irradiator.

(F) Distinct focal luminescence was visualized away from the injection site near the animal's axillary and brachial lymph nodes.

(A and B) reproduced with permission from Zhang et al. (Zhang et al., 2019b). Copyright 2019, Wiley-VCH. (C and D) reproduced with permission from Zhang et al. (Zhang et al., 2019a). Copyright 2019, Wiley-VCH. (E and F) reproduced with permission from Naczynski et al. (Naczynski et al., 2015). Copyright 2014, American Chemical Society.

from 270 to 420 nm. Subsequently, Zhu et al. (2020) also reported $CsPbCl_3$:Er^{3+}, Yb^{3+} QDs with NIR-II emission of Er^{3+} ions upon 365-nm excitation.

For Ln^{3+} sensitization, a new class of NIR-II luminescent nanoprobes of CaS: Ce^{3+}, Er^{3+}/Nd^{3+} NPs was recently reported by our group (Zhang et al., 2019b). The NIR-II luminescence of Er^{3+} and Nd^{3+} was realized through sensitization of Ce^{3+} (Figures 4A and 4B), which can be effectively excited using a low-cost blue light-emitting diode chip. With the rapid development of NIR optical imaging, there is an increased demand for the NIR-II luminescent probes with the excitation light located in the NIR region. In such NIR region, the excitation light with low water absorption and tissue overheating is more favorable for *in vivo* imaging. To address this concern, attempts were made to enrich excitation wavelengths by employing NIR-excitable Ln^{3+} ions as sensitizers, including Nd^{3+}, Er^{3+}, and Tm^{3+}. Nd^{3+} has multiple absorption positions and relatively large cross-section compared to Yb^{3+}. Utilizing Nd^{3+} as a sensitizer, the excitation wavelength can be shifted to 808 nm (Wang et al., 2013). Water absorption is much lower with an absorption

coefficient of 0.02 cm^{-1} at 808 nm, in contrast to 0.48 cm^{-1} at 980 nm. Accordingly, the laser-induced tissue heating effect was minimized. It should be noted that Yb^{3+} are generally doped into Nd^{3+}-sensitized NPs as bridging ions to guarantee the efficient sensitization. Based on this concept, a series of NIR-II Nd^{3+}/Yb^{3+}/Ln^{3+} doped NPs, such as $NaGdF_4$:Yb^{3+}, Nd^{3+}, Tm^{3+} (Tan et al., 2018), $NaGdF_4$:Nd^{3+}@$NaGdF_4$:Tm^{3+}, Yb^{3+} (Wang et al., 2014), and $NaGdF_4$@Na(Gd, Yb)F_4:Er^{3+}@$NaYF_4$:Yb^{3+}@$NaNdF_4$:Yb^{3+} (He et al., 2015), were further proposed.

Besides Nd^{3+}-sensitized NPs, a series of Er^{3+}-sensitized NPs have also been reported. Wang et al. (2018d) described a class of NIR-II luminescent nanoprobes of $NaErF_4$:Yb^{3+}@$NaLuF_4$, which can be efficiently excited at ~800 nm, benefiting from the self-sensitization process of Er^{3+} ions. To open new possible avenues for deep tissue imaging, the decent absorption peak of Er^{3+} at ~1530 nm is adopted to expand the excitation wavelength in the NIR-II region. As a typical example, the $NaErF_4$:Ln^{3+}@$NaYF_4$ (Ln^{3+} = Ho^{3+} or Nd^{3+}) NPs were proposed (Liu et al., 2018). Er^{3+} was acting as both sensitizer and emitter to harvest pump photons at 1530 nm and then promote the emission at 980 nm, while the Ho^{3+} or Nd^{3+} dopants served as emitters to generate the NIR-II emission at 1180 nm or 1060 nm, respectively.

As a new alternative of sensitizers, Tm^{3+} can absorb the NIR excitation photons at 1208 nm and 808 nm and transfer excitation energy to activators. Upon 1208-nm excitation, $NaYF_4$:Tm^{3+}, Er^{3+}@$NaYF_4$ NPs were demonstrated to produce 1525 nm NIR-II luminescence from Tm^{3+} sensitizer to Er^{3+} emitter via the efficient ET process (Figures 4C and 4D) (Zhang et al., 2019a). Upon 808-nm excitation, Ho^{3+} emitter showed the NIR-II emission at 1180 nm in $NaYF_4$: Tm^{3+}, Ho^{3+}@$NaYF_4$ NPs.

Besides NIR light source, X-ray has become a promising new excitation source to produce NIR-II emission (Figures 4E and 4F) (Naczynski et al., 2015). The X-ray excitation allows probes to be excited at essentially any depth in the human body, eliminates the background signal generated by tissue autofluorescence, and simplifies image reconstruction for optical tomography. For instance, $NaYF_4$:Yb^{3+}, Er^{3+} NPs were demonstrated to generate a distinct NIR-II emission peak centered at ~1530 nm after X-ray irradiation and show their potential for deep tissue imaging applications. However, few X-ray excitable Ln^{3+}-containing NIR-II nanoprobes have been reported. Much work is still needed to exploit X-ray excitable Ln^{3+}-containing nanoprobes with bright NIR-II luminescence.

Emission manipulation

Benefiting from the rich energy levels, abundant wavelengths of Ln^{3+} in the NIR-II region can be achieved. In addition, Ln^{3+} ions typically exhibit much narrower emission band widths than that of QDs and organic dyes, which can reduce signal interference in both *in vivo* bioimaging and *in vitro* biodetection. As such, many efforts have been devoted to manipulating NIR-II emission to meet the requirements for the proposed applications.

For example, Nd^{3+}-doped $NaGdF_4$ NPs showed three PL bands peaking at 900, 1050, and1330 nm upon 740-nm excitation, which were assigned to the transitions from $^4F_{3/2}$ to ^4I_J (J = 9/2, 11/2, 13/2) (Chen et al., 2012). These NIR emissions within "optical transparency window" were exceptionally sharp, which made $NaGdF_4$:Nd^{3+} NPs an ideal luminescent probe for high-contrast *in vivo* imaging. Besides Nd^{3+} ions, Pr^{3+} ($^1G_4 \rightarrow {}^3H_5$), Ho^{3+} ($^5I_6 \rightarrow {}^5I_8$), Er^{3+} ($^4I_{13/2} \rightarrow {}^4I_{15/2}$), and Tm^{3+} ($^3H_4 \rightarrow {}^3F_4$) also show great potential for constituting NIR-II luminescent materials because their emissions are located in the spectral region of 1000–1700 nm (Figures 5A–5C) (Naczynski et al., 2013). By utilizing these Ln^{3+} ions, NIR-II luminescent probes with multicolor emissions were designed for applications in multispectral imaging and multiplexed biodetection.

Ratiometric optical nanoprobes are favorable for providing an increased signal-to-background ratio and more reliable results in bioimaging and biosensing. With the development of these ratiometric nanoprobes, several Ln^{3+}-containing NIR-II luminescent materials with two or multiple non-overlapped emissions were designed. For example, $NaErF_4$:Ho^{3+}@$NaYF_4$ NPs emitted efficient emission at 1180 nm upon 1530-nm excitation (Figures 5D–5F) (Liu et al., 2018). Acting as both sensitizer and emitter, Er^{3+} showed emissions peaked at 650 nm ($^4F_{9/2} \rightarrow {}^4I_{15/2}$) and 980 nm ($^4I_{11/2} \rightarrow {}^4I_{15/2}$), respectively. Meanwhile, the emission peaked at 1180 nm was also detected due to the ET process from Er^{3+} to Ho^{3+}. By taking advantage of the NIR emissions of Er^{3+} and Ho^{3+}, novel ratiometric luminescent (I_{980}/I_{1180}) nanoprobes were designed for *in vivo* inflammation dynamic detection.

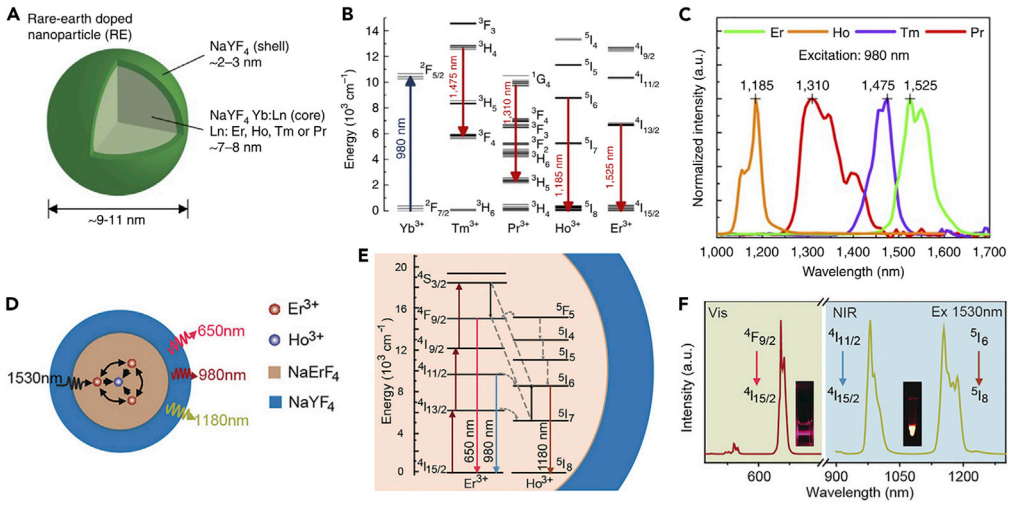

Figure 5. Emission manipulation of Ln^{3+}-containing NIR-II luminescent nanoprobes

(A) Rare-earth nanoprobes consist of a $NaYF_4$:Yb^{3+}, Ln^{3+} core (Ln^{3+}: Er^{3+}, Ho^{3+}, Tm^{3+} or Pr^{3+}) surrounded by an undoped shell of $NaYF_4$.

(B) NIR-II emissions from different Ln^{3+} emitters like Ho^{3+}, Pr^{3+}, Tm^{3+}, and Er^{3+}.

(C) 1185, 1310, 1475, and 1525 nm emissions of Ho-, Pr-, Tm-, and Er-doped NPs are attributed to the $^5I_6 \rightarrow {}^5I_8$, $^1G_4 \rightarrow {}^3H_5$, $^3H_4 \rightarrow {}^3F_4$, and $^4I_{13/2} \rightarrow {}^4I_{15/2}$ transitions, respectively.

(D) Schematic illustration of the ET in the $NaErF_4$:Ho^{3+}@$NaYF_4$ NPs.

(E) Simplified energy levels of Er^{3+}, Ho^{3+} in $NaErF_4$:Ho^{3+}@$NaYF_4$ NPs, showing the proposed ET process through sensitization of Er^{3+}.

(F) Emission spectra of the obtained NIR-II NPs.

(A–C) reproduced with permission from Naczynski et al. (Naczynski et al., 2013). Copyright 2013, Springer Nature. (D–F) reproduced with permission from Liu et al. (Liu et al., 2018). Copyright 2018, Wiley-VCH.

Photoluminescence lifetime manipulation

The PL lifetime is an important parameter for Ln^{3+}-containing NPs. Recently, the time-domain NIR-II nanoprobes show enormous potential in bioimaging because PL lifetime can avoid inhomogeneous signal attenuation in biological tissues. As such, Ln^{3+}-doped NIR-II NPs with engineered PL lifetime were developed through controlling their structure and composition.

The nonradiative relaxation caused by surface defects may significantly affect the PL lifetime of Ln^{3+}-containing NPs. By virtue of efficient surface passivation treatment, time-domain luminescent NPs were obtained by coating an inert shell on the Ln^{3+}-containing NPs. For instance, the PL lifetime of the core-shell α-$NaYbF_4$@CaF_2 NPs with NIR emission can be tuned from 33 μs to 2.18 ms by controlling the thickness of CaF_2 shells (Gu et al., 2019). It was determined that the optimal thickness of the CaF_2 inert shell was 2.6 nm, which was sufficient to overcome the surface-quenching-induced concentration quenching. Correspondingly, the PL lifetime was prolonged close to the radiative lifetime of Yb^{3+}.

In 2018, Fan et al. (2018) proposed a systematic approach to tune the PL lifetime by controlling the energy relay in a core/multi-shell structure (Figures 6A–6C), which consisted of four components, including the inert core ($NaGdF_4$), the activation layer ($NaGdF_4$:Yb^{3+}, Er^{3+}), the energy relay layer ($NaYF_4$:Yb^{3+}), and the outer absorption layer ($NaNdF_4$:Yb^{3+}). These core/multi-shell NPs absorbed 808-nm photons to generate emission centered at 1525 nm through efficient $Nd^{3+} \rightarrow Yb^{3+} \rightarrow Er^{3+}$ ET process. The lifetime-engineering was accomplished in two directions. One was prolonging the average process from absorption to emission through increasing the thickness of the energy relay layer, leading to a longer PL lifetime. The other was accelerating the conversion of stored energy into PL emission via increasing the Er^{3+} concentration, which shortened the PL lifetime. As a result, the PL lifetime of Er^{3+} at 1525 nm can be tuned spanning three orders of magnitude. Based on these NPs, more than 10 distinct lifetime identities were clearly distinguished using a TR imaging system. Likewise, tunable lifetimes were achieved for other NIR-II Ln^{3+} ions, including Ho^{3+} with emission at 1155 nm, Pr^{3+} with emission at 1289 nm, Tm^{3+} with emission at 1475 nm, and Nd^{3+} with emission at 1060 nm.

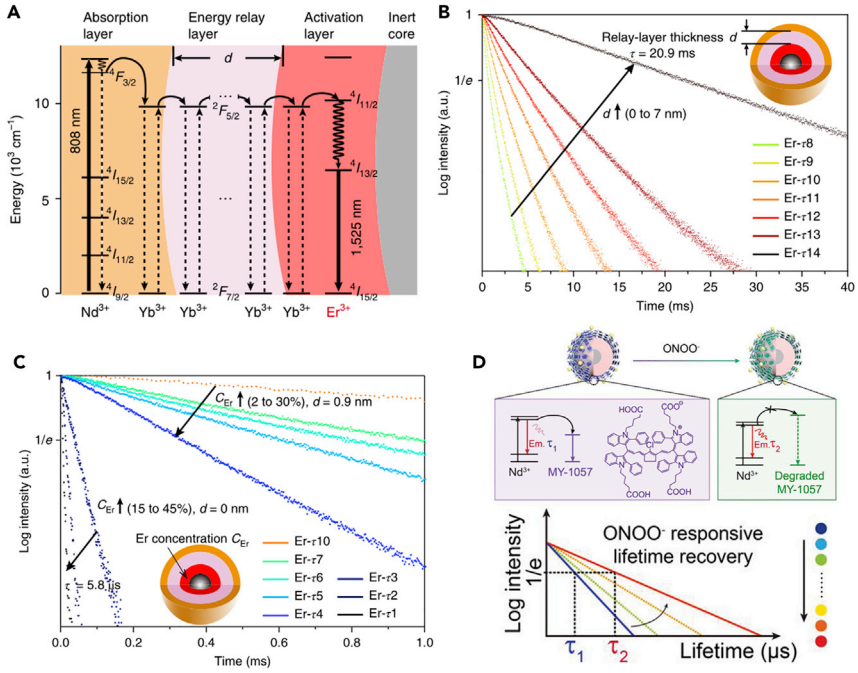

Figure 6. PL lifetime manipulation of Ln^{3+}-containing NIR-II luminescent nanoprobes

(A) Energy level diagram illustrating the luminescence process of the Er^{3+}-doped core/multi-shell NPs.

(B) PL decays measured at 1525 nm from the as-prepared NPs with energy relay shells of increasing thickness (D) from 0 to 7 nm.

(C) PL decays of the NPs with increased Er^{3+} doping concentration (C_{Er}) from 2 mol% to 30 mol% for d = 0.9 nm and from 15 mol% to 45 mol% for d = 0 nm.

(D) Schematic illustration of PL lifetime detection of reactive nitrogen species based on Ln^{3+}–cyanine FRET nanoprobes.

(A–C) reproduced with permission from Fan et al. (Fan et al., 2018). Copyright 2018, Springer Nature. D reproduced with permission from Zhao et al. (Zhao et al., 2020). Copyright 2020, Wiley-VCH.

Besides manipulating core-shell structures of the Ln^{3+}-doped NPs, the incorporation of NIR-II dye with Ln^{3+}-doped NPs may provide an efficient ET pathway to tune PL lifetime of Ln^{3+}. Zhao et al. (2020) reported a Förster resonance energy transfer (FRET) nanoprobe for quantitative luminescence-lifetime biosensing by employing the NIR-II dye MY-1057 encapsulated β-$NaYF_4$@$NaYF_4$:Nd^{3+} NPs (Figure 6D). In these nanoprobes, β-$NaYF_4$@$NaYF_4$:Nd^{3+} NPs were utilized as FRET donor with emission at 1060 nm, while MY-1057 was used as energy acceptor. Because of the Ln^{3+}–cyanine FRET process, the PL lifetime of Nd^{3+} may be decreased from 305 to 75 μs with the addition of MY-1057. The structure of MY-1057 degraded in response to reactive nitrogen species, subsequently leading to the lifetime recovery.

Photoluminescence intensity improvement

Currently, the low PL intensity of Ln^{3+}-containing NIR-II NPs owing to the small absorption cross-section of Ln^{3+} has been the major bottleneck for their commercial bioapplications. To this regard, researchers tried their best to design efficient Ln^{3+}-containing NIR-II luminescent nanoprobes through spatial distribution of dopants, effective surface passivation, manipulating the ET pathways, and optimizing host matrix, etc.

Theoretically, high doping concentration of Ln^{3+} ions provides more emitters, which might favor the light absorption and emitting. However, the high doping will unavoidably cause localized concentration quenching of sensitizers or activators. Therefore, overcoming concentration quenching at high dopant concentration has become an urgent task for improved PL intensity.

Generally, concentration quenching is attributed to deleterious cross-relaxation between dopant ions in close proximity. Through manipulating the spatial distribution of the doped Ln^{3+} ions, the NIR-II emission identity can be improved. For example, considering the short spatial distances between Tm^{3+} and Nd^{3+} ions may aggravate the quenching of the NIR-II emission from Nd^{3+} at a high local concentration. The

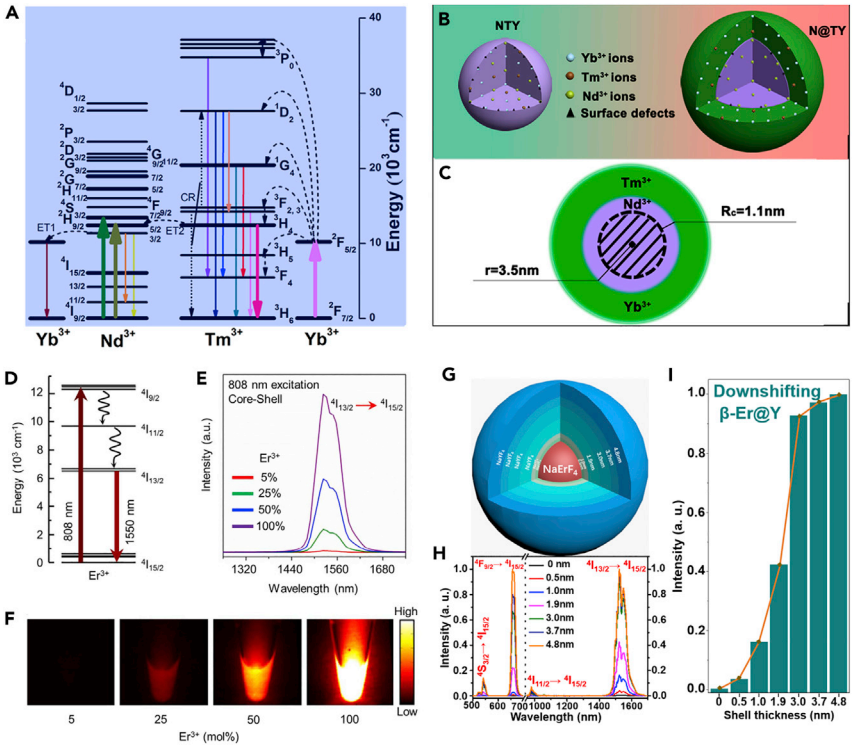

Figure 7. PL intensity improvement of Ln^{3+}-containing NIR-II luminescent nanoprobes through core-shell structure design

(A) Energy level diagrams of Nd^{3+}, Tm^{3+}, and Yb^{3+} ions in $NaGdF_4$:Nd^{3+}@$NaGdF_4$:Tm^{3+}, Yb^{3+} NPs.

(B and C) Illustration of (B) the spatial structure and (C) cross-section of the core-shell structure with spatial isolated doping.

(D) Energy level diagram of Er^{3+} in β-$NaErF_4$@$NaLuF_4$ NPs, showing the excitation (808 nm) and the emission (1550 nm) levels.

(E) Emission spectra of $NaErF_4$@$NaLuF_4$ NPs with variable Er^{3+} dopant concentrations in the core, showing emission between 1450 and 1650 nm upon 808-nm excitation.

(F) NIR-II emission images from colloidal dispersion of $NaErF_4$@$NaLuF_4$ NPs (λ_{ex} = 808 nm) in the region of 0.9–1.7 μm, showing emission enhancement with the increase in dopant concentration.

(G) Schematic illustration of β-$NaErF_4$@$NaYF_4$ NP with varying shell thicknesses. (H) Dependence of emission spectra of $NaErF_4$@$NaYF_4$ NPs on the shell thickness varying from 0 to 4.8 nm.

(I) NIR-II intensity integrated from 1400 to 1700 nm versus the shell thickness for $NaErF_4$@$NaYF_4$ NPs. All the emission spectra were acquired upon laser excitation at 808 nm with an output power density 0.66 W/cm^2.

(A–C) reproduced with permission from Zhou et al. (Zhou et al., 2013). Copyright 2013, American Chemical Society. (D–F) reproduced with permission from Johnson et al. (Johnson et al., 2017). Copyright 2017, American Chemical Society. G-I reproduced with permission from Li et al. (Li et al., 2020a). Copyright 2020, American Chemical Society.

spatial isolation was carried out to shield the unwanted ET process between Tm^{3+} and Nd^{3+} ions (Figures 7A–7C) (Johnson et al., 2017). As a result, the core-shell $NaGdF_4$:Nd^{3+}@$NaGdF_4$:Tm^{3+}, Yb^{3+} NPs were synthesized with the optimized NIR-to-NIR emission intensity, which was increased by at least a factor of 7 as compared with the $NaGdF_4$:Nd^{3+}, Tm^{3+}, Yb^{3+} counterparts.

Besides cross-relaxation between Ln^{3+} ions, the energy migration from Ln^{3+} to the defects may also deteriorate the NIR-II emission of Ln^{3+} ions. Therefore, the epitaxial growth of a shell is widely adopted to spatially isolate the core with surface defects. It was demonstrated that in $NaYF_4$:Er^{3+} NPs, the major quenching process at high dopant concentrations predominantly originated from energy migration from Er^{3+} to the surface rather than cross-relaxation between dopants (Johnson et al., 2017). After coating with an inert $NaLuF_4$ shell, the intense NIR-II emission of Er^{3+} was achieved (Figures 7D–7F). In their work, the NIR-II luminescence peaked at 1525 nm, corresponding to the $^4I_{13/2} \rightarrow {}^4I_{15/2}$ transition of Er^{3+}, was enhanced by ~659 times relative to that of their parent core-only NPs.

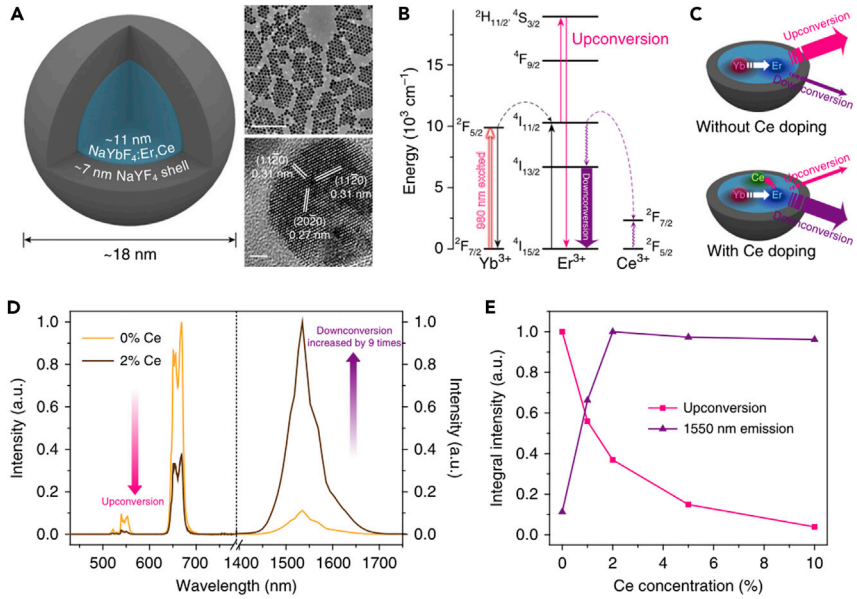

Figure 8. Improvement of Ln^{3+}-containing NIR-II luminescent nanoprobes through cation incorporation

(A) Schematic design of core-shell $NaYbF_4$:Er^{3+}, Ce^{3+}@$NaYF_4$ NP (left) with corresponding large scale TEM image (upper right, scale bar = 200 nm) and HRTEM image (lower right, scale bar = 2 nm).

(B) Simplified energy-level diagrams depicting the ET process between Yb^{3+}, Er^{3+}, and Ce^{3+} ions.

(C) Schematic illustration of the proposed ET mechanisms in $NaYbF_4$:Er^{3+}@$NaYF_4$ NPs with and without Ce^{3+} doping.

(D) PL emission spectra of the $NaYbF_4$:Er^{3+}@$NaYF_4$ NPs with 0 and 2 mol% Ce^{3+} doping.

(E) Schematic representation of Ce^{3+} doping concentration and corresponding upconversion and NIR-II emission intensity of $NaYbF_4$:Er^{3+}, Ce^{3+}@$NaYF_4$ NPs upon 980-nm excitation.

Reprinted with permission from Zhong et al. (Zhong et al., 2017). Copyright 2017, Springer Nature.

Inspired by this work, Li et al. (2020a) revealed the shell thickness effect on the NIR-II luminescence from the $NaErF_4$@$NaYF_4$ NPs through elaborately modulating the shell thickness (Figures 7G–7I). As the shell thickness increasing from 0.5 to 3 nm, the NIR-II luminescence intensity of Er^{3+} was enhanced gradually and showed a steady value for shell thickness over 3 nm. Finally, the absolute PLQY of $NaErF_4$@$NaYF_4$ NPs with the shell thickness of 3 nm was determined to be 10.2 $\pm$ 0.8% upon 808-nm laser excitation with power density of 0.1 W/cm^2. Apart from the utilization of shells with similar lattice parameters of the core, silica shell coating was adopted to suppress the vibrational quenching caused by the O–H groups and improve the NIR-II emission. For example, the NIR-II emission intensity of NdF_3 NPs was enhanced by ~1.6 times after coating the SiO_2 shell (Yu et al., 2008).

In addition to inorganic shells, organic dye molecules were also attached to the surface of Ln^{3+}-containing NPs for efficient NIR-II emitting. Typically, indocyanine green, as the light-harvesting surface ligand, was employed to sensitize $NaYF_4$:Er^{3+} NPs (Wang et al., 2018a). Likewise, the named dye HC-Ni, which can be activated by glutathione (GSH), was modified on the surface of $NaYF_4$:Yb^{3+}, Er^{3+}@$NaYF_4$:Nd^{3+} NPs via hydrophobic interaction (Li et al., 2020c). With the addition of GSH, the NIR-II emission intensity of dye-modified NPs was markedly increased due to the target-triggered dye-sensitization process.

Another efficient way to enhance NIR-II luminescence is manipulating the ET pathways through cation incorporation. Specifically, in the core-shell $NaErF_4$:Yb^{3+}@$NaLuF_4$ NPs, the doped Yb^{3+} ions acting as energy trapping centers, can induce back ET to populate the $^4I_{13/2}$ level of Er^{3+} (Wang et al., 2018d). As a result, $NaErF_4$@$NaLuF_4$ with 20 mol% Yb^{3+} generated efficient NIR-II luminescence at 1525 nm with optimized PLQY of ~11% (emission range: 900–1700 nm) upon 808-nm excitation. In addition, Ce^{3+} was doped into Er^{3+}-based NPs to boost the NIR-II emission of Er^{3+}. Zhong et al. (2017) reported a NIR-II luminescence nanoprobe of core-shell $NaYbF_4$:Er^{3+}@$NaYF_4$:Ce^{3+} NPs (Figure 8). The nonradiative phonon-assisted cross-relaxation of $^4I_{11/2} \rightarrow {}^4I_{13/2}$ of Er^{3+} was facilitated by the Ce^{3+} dopants due to the small mismatch of energy level between Ce^{3+} and Er^{3+} ions, which enhanced the population of the $^4I_{13/2}$ level of Er^{3+}.

Correspondingly, an increased NIR-II luminescence was achieved. In the presence of Ce^{3+} ions, the NIR-II luminescence of Er^{3+} was found to be 9-fold higher than that without Ce^{3+} doping. However, the low concentration of Ce^{3+} with only 2 mol% limited the further improvement of NIR-II PLQY. To this regard, our group synthesized $NaCeF_4$:Er^{3+}, Yb^{3+}@$NaCeF_4$ NPs (Lei et al., 2018). Upon excitation at 980 nm, the Ce^{3+} in the host lattice significantly enhanced the NIR-II luminescence of Er^{3+} at 1530 nm with a maximum NIR-II QY of 32.8%, which is the highest among Er^{3+}-activated inorganic nanoprobes.

SURFACE FUNCTIONAL MODIFICATION

The as-prepared Ln^{3+}-containing NIR-II luminescent nanoprobes are usually capped with hydrophobic ligands, which thus limit their bioapplications where hydrophilicity is a prerequisite. As a consequence, one crucial issue for the bioapplications of the hydrophobic Ln^{3+}-containing NIR-II luminescent materials is the surface functional modification, in an effort to render them water-soluble and provide reactive groups for subsequent bioconjugation to various biomolecules. To this end, a variety of surface modification strategies like inorganic shell coating, organic polymer modification, and biofunctional agent conjugation have been developed over the past decade, as will be briefly overviewed in this section.

Inorganic shell coating

Inorganic shells are frequently used to minimize the PL quenching of emitters from the surface ligands and liquid media. Meanwhile, some inorganic materials also endow the Ln^{3+}-containing NIR-II luminescent nanoprobes with good hydrophilicity. Generally, the inorganic shells can be classified as amorphous inorganic shells and crystalline inorganic shells. The amorphous inorganic shells with large surface area and tunable pore sizes can serve as efficient carriers for drug delivery and release. As a typical kind of amorphous inorganic shells, silica attracted considerable attention for bioapplications owing to its controllable synthesis, facile modification, and excellent biocompatibility. For instance, the $NaGdF_4$:Nd^{3+}@$NaGdF_4$ NPs were coated by mesoporous SiO_2 for delivering drugs (Wang et al., 2017b). Moreover, the silica shells can be functionalized with molecular, supramolecular or polymer moieties, which provides the nanoprobes with more exciting opportunities for multimodal biosensing. Specifically, photosensitizing molecules can be embedded into mesoporous SiO_2 shell for NIR-II luminescent-based photodynamic therapy applications (Tang et al., 2011). In addition, complexes that have potential in biodetection and bioimaging can be covalently linked with the silica shell to impart the nanoprobes with new functional features. For example, Gd^{3+} complex can endow $NaLuF_4$:Yb^{3+}, Tm^{3+} NPs with T_1-enhanced magnetic resonance, which holds the promise for both NIR luminescence imaging and magnetic resonance imaging (Xia et al., 2012).

The crystalline inorganic shells are generally prepared through epitaxial growth method. They have desirable properties such as ideal optical transparency and high crystallizability. These intriguing properties make them useful for minimizing the surface-related quenching effect of NIR-II NPs and improve resistance to aqueous quenchers (*e.g.*, -OH, $-NH_2$). However, most crystalline inorganic shells are mainly restricted by the poor biocompatibility and monotonous function. Hence, it is desired to exploit the crystalline inorganic shells with good water dispersibility and superior biocompatibility. Compared with the most used $NaYF_4$, CaF_2 shell is more biocompatible because it is an endogenous component in live systems. Therefore, CaF_2 was reported as the epitaxial shell to preserve the efficient luminescence of α-$NaYbF_4$ (Gu et al., 2019), $NaYF_4$:Yb^{3+}, Tm^{3+} NPs (Shen et al., 2013), and $NaLuF_4$:Yb^{3+}, Ln^{3+} (Ln^{3+} = Er^{3+}, Ho^{3+}, Tm^{3+}) (Li et al., 2017) in biological media.

Recently, our group reported a novel strategy to confer Ln^{3+} with target recognition ability and customizable surface attributes, based on the good biocompatibility and unique surface chemistry of single-layer graphene oxide (GO) (Figure 9) (Song et al., 2019). GO coating endowed $NaYF_4$:Yb^{3+}, Er^{3+}@$NaYF_4$ NPs with amphiphilicity and high specific surface areas, thereby enabling them to be well dispersed in diverse solvents and stably modified with various agents through non-covalent interactions. In this work, the GO-coated NPs were functionalized with DNA for intracellular tracking and microRNA visualization. Moreover, the protein can be armored on these GO coated NPs for tumor-targeted NIR-II imaging.

Organic polymer modification

Organic polymers are the most frequently used agents for surface engineering of Ln^{3+}-containing NIR-II nanoprobes. To ensure the stable binding between organic polymers and inorganic NPs, three well-known

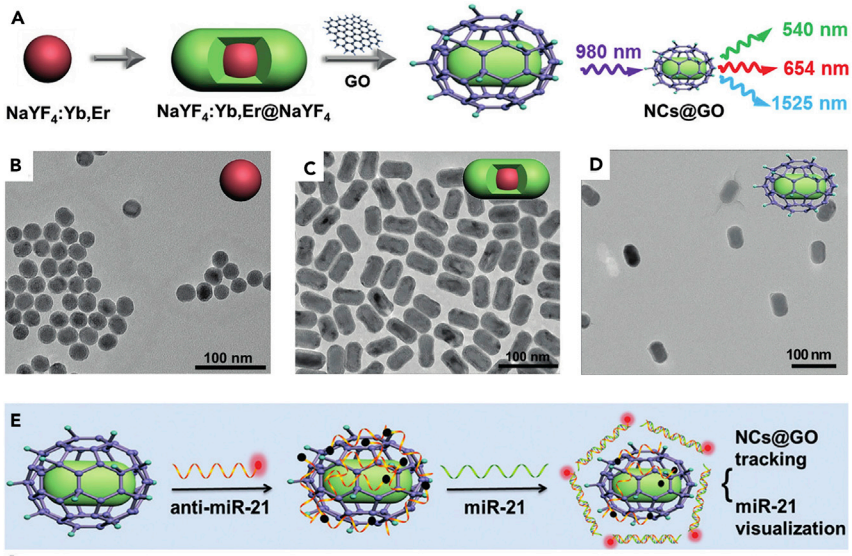

Figure 9. GO coated Ln^{3+}-containing NIR-II luminescent nanoprobes

(A) Schematic of the synthesis of NPs@GO.

(B–D) TEM images of (B) core-only $NaYF_4$:Yb^{3+}, Er^{3+}, (C) core-shell $NaYF_4$:Yb^{3+}, Er^{3+}@$NaYF_4$, and (D) NPs@GO.

(E) Schematic of the design and imaging principle of the nanoprobe.

Reproduced with permission from Song et al. (Song et al., 2019). Copyright 2019, Wiley-VCH.

strategies have been proposed (Figure 10): (1) surface ligand exchange; (2) surface ligand attraction; (3) layer-by-layer electrostatic assembly.

Hitherto, a number of organic polymers have been developed for surface engineering of Ln^{3+}-containing NIR-II nanoprobes. Among them, polyethylene glycol (PEG) is the most widely adopted and has been approved by FDA for human oral, intravenous, and dermal pharmaceutical applications. PEG molecules can be transformed into amphipathic molecules through organic synthesis, resulting in hydrophobic groups as well as hydrophilic groups. For instance, the hydrophobic groups can be diphosphate, distearoyl phosphoethanolamine (DSPE), poly (lactic-co-glycolic acid), etc., while the hydrophilic groups can be carboxyl (COOH), maleimide, amidogen (NH_2), etc (Li et al., 2013). Being amphiphilic, nontoxic, non-immunogenic and non-antigenic, PEG as modifying polymer can markedly improve the water solubility and biocompatibility of Ln^{3+}-containing NIR-II luminescent nanoprobes. The hydrophobic portion of amphiphilic PEG polymers usually interacts with the organic capping layer of NPs via hydrophobic attraction, while the hydrophilic portion faces outwards, interacting with the aqueous solvent and rendering the particle water soluble, which is called the "surface ligand attraction" strategy. Typically, the amphiphilic 1,2-distearoyl-sn-glycero-3-phosphoethanolamine-N-[carboxy-(polyethyleneglycol)-2000] (DSPE-PEG2000-COOH) phospholipids were used to coat the multi-shell $NaGdF_4$@Na(Gd, Yb)F_4:Er^{3+}@$NaYF_4$:Yb^{3+}@$NaNdF_4$:Yb^{3+} NPs for NIR-II *in vivo* bioimaging via the surface ligand attraction strategy (Wang et al., 2014). The NPs can be easily transferred from the organic phase to the aqueous phase and remained excellent monodisperse. Moreover, the rich and adjustable functional groups render PEGylation suitable for various applications. For example, folic acid (FA), whose receptor overexpressed in cancer cells, was coupled onto the surface of the PEGylation NPs through covalent conjugation (Li et al., 2019c). The obtained NPs/FA conjugate was demonstrated to be a tumor-targeted NIR-II probe for simultaneously visualizing both subcutaneous and intraperitoneal tumor xenografts *in vivo*.

A series of other organic polymers such as polyacrylic acid (PAA), polydopamine (PDA), and polyvinyl alcohol were also employed for the surface modification of Ln^{3+}-containing NIR-II luminescent NPs. Zhang et al. (2007) first reported the use of ligand exchange strategy to convert oleic acid capped NPs into hydrophilic NPs. In a typical ligand exchange procedure, the original capping ligand of oleic acid on the surface of $NaLuF_4$:Gd^{3+}, Nd^{3+} NPs can be replaced with PAA (Li et al., 2019a). These PAA-modified $NaLuF_4$:Gd^{3+}, Nd^{3+} NPs were observed to accumulate in the reticuloendothelial system and excreted through the hepatic

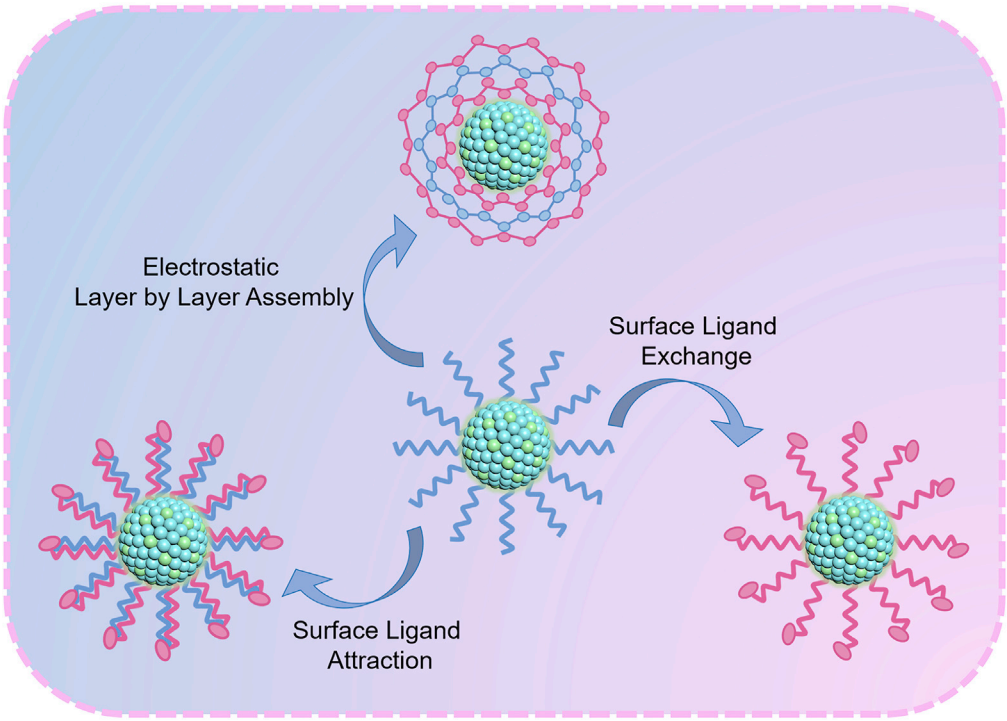

Figure 10. Typical surface engineering strategies for making hydrophilic and biocompatible Ln^{3+}-containing NIR-II luminescent nanoprobes with organic polymers

pathway. In another work, Dai et al. (2017) found that the thicker PDA layer covered on the $NaYF_4$:Nd^{3+}@-$NaLuF_4$ may enhance photothermal conversion efficiency of the resulting nanocomposites. Subsequently, Li et al. (2019b) exhibited non-invasive angiography of vascular malformations/tumors using $NaLnF_4$@PDA nanoprobes in the brain/abdomen of mice.

Biofunctional agent conjugation

Although surface coating of Ln^{3+}-containing NIR-II nanoprobes with inorganic shells or organic polymers has been demonstrated to improve their biocompatibility, the targeting efficiency is still unsatisfied because of the poor accumulation ability and insufficient retention time. Hence, the surface engineering with bioactive agents such as antibodies (You et al., 2018), DNA strings (Dumont et al., 2012), cancer cell membrane (Zhang et al., 2020b), and viruses (Zhang et al., 2017) was developed, which can significantly improve the selectivity of Ln^{3+}-containing NIR-II nanoprobes toward specific targets and enhance their targeting efficiency. For instance, human serum albumin (HSA) was modified on the surface of $NaYF_4$:Yb^{3+}, Er^{3+}@$NaYF_4$ NPs and magnified the accumulation of the NPs in tumor tissue by more than 10 times as compared with the uncoated counterparts (Naczynski et al., 2013). Furthermore, by controlling the thickness of albumin encapsulation, the biodistribution of the NPs can be modulated.

In current NIR-II luminescent imaging-guided surgery practice, photostable probes with long tumor retention period are favorable. Accordingly, Wang et al. (2018b) reported that the *in vivo* assembly of

complementary DNA modified $NaGdF_4:Nd^{3+}@NaGdF_4$ nanoprobes may alter the tumor retention kinetics in a good manner and improve staging and debulking efforts in surgery. In their work, the ligand exchange strategy was utilized to realize the surface functionalization of $NaGdF_4:Nd^{3+}@NaGdF_4$ NPs with complementary DNA. After being covalently anchored with the specific tumor peptide for improved targeting efficiency, these nanoprobes that can assemble efficiently, showed great potential in the application for intraoperative tumor-specific NIR-II imaging. Recently, cancer cell membrane was reported to modify $NaYF_4:Nd^{3+}@NaYF_4$ nanoprobes for improved performance in tumor detection and tumor surgery navigation. Cancer cell membrane can camouflage nanoprobes to avoid fast clearance and macrophage (Zhang et al., 2020b). Thus, such cancer-cell-membrane coated nanoprobes exhibited significantly higher accumulation in the tumor and significantly enhanced blood retention compared to the counterparts with PEG encapsulation. These NIR-II nanoprobes with good tumor targeting ability further improved the tumor imaging quality in NIR-II imaging-guided surgery, showing the potential for clinical translation.

For *in vivo* molecular imaging, the non-invasive visualization of the disease biomarker can be realized by the conjugation of antibodies to Ln^{3+}-containing NIR-II luminescent nanoprobes. As an example, AMD-3100 can be adsorbed onto the surface of above-mentioned HSA coated $NaYF_4:Yb^{3+}$, $Er^{3+}@NaYF_4$ NPs to further target the cancer biomarker of CXCR4 (Kantamneni et al., 2017). Thus, the AMD-3100 modified nanoprobes can label the lesions at distinct organ sites. In another example, amine groups modified $NaYbF_4:Er^{3+}$, Ce^{3+}, $Zn^{2+}@NaYF_4$ NPs were conjugated with anti-PD-L1 mAb (*i.e.*, monoclonal anti-bodies of Programmed Cell Death-Ligand 1) through 1-(3-dimethylaminopropyl)-3-ethylcarbodiimide hydrochloride (EDC) chemistry (named ErNPs-aPDL1) (Zhong et al., 2019). This ErNPs-aPDL1 NIR-II nanoprobe was employed for dynamic monitoring and assessing of PD-L1 heterogeneity in tumor. Furthermore, the agents that involve in biochemical reactions related to the biomarkers of physiological abnormalities can also be conjugated to Ln^{3+}-containing NIR-II nanoprobes. For example, GSH that can respond to reactive oxygen species was selected to functionalize $NaGdF_4:Nd^{3+}@NaGdF_4$ NPs for the precise bioimaging of inflammation (Zhao et al., 2019).

SUMMARY AND OUTLOOK

Ln^{3+}-containing NIR-II luminescent nanoprobes have received extensive interest in recent years because of their excellent physicochemical characteristics, which make them intriguing candidates for diverse areas of bioimaging, biosensing, and imaging-guided therapy. Their optical properties can be modulated through tailoring a variety of parameters. As a result, this novel class of luminescent nanoprobes, while being in its infancy, has been rapidly developed and pushed forward to a new horizon for bioapplications in the NIR-II region. Substantial progresses have been gained from their fundamental photophysics to ingenious design strategies. Nevertheless, it remains several challenges to be solved in an effort to fulfill the requirements of commercial applications.

First, the NIR-II luminescence of Ln^{3+}-containing nanoprobes results from several ET pathways due to the rich energy levels of Ln^{3+} and complex crystal environment. Therefore, a comprehensive investigation of the excited-state dynamics of Ln^{3+} is a prerequisite for rationally modulating and optimizing the optical properties of Ln^{3+}-containing nanoprobes. To this end, fundamental studies through the high-resolution PL spectroscopy, time-resolved PL spectra, transient absorption spectra are urgently needed to elucidate the relationship between the composition/microstructure of the hosts and NIR-II luminescence of Ln^{3+} ions.

Second, one of the key bottlenecks for Ln^{3+}-containing NIR-II nanoprobes is the relatively low PLQYs caused by the intrinsic low absorption cross section of Ln^{3+}, which may cause poor temporal resolution and low sensitivity of biosensing. It should be noted that most of the current hosts are relatively inert, which are incapable of sensitizing the NIR-II luminescence of Ln^{3+} emitters. As such, there is still much room to optimize the optical properties of Ln^{3+}-containing NIR-II nanoprobes. Sustainable efforts should be paid to explore more innovative hosts (*e.g.*, QDs, metal-organic frameworks) and sensitization strategies so as to improve the PLQY of Ln^{3+}-containing NIR-II nanoprobes. In addition, lifetime-engineered luminescent nanoprobes are getting rising attention in multiplexing imaging for eliminated signal loss and distortion in deep tissues. Nevertheless, approaches for lifetime probes with excellent sensitivity and fast feedback are lacking of exploiting. To seek the way, continuous efforts are needed to work on the precise synthesis and controlled lifetime responsiveness of these probes.

Thirdly, for Ln^{3+}-containing NIR-II nanoprobes, their biocompatibility and long-term toxicity are the key factors for clinical translation, which still lack thorough investigations. A systematic and general standard should be established to evaluate the performance of these probes *in vivo*. Although various surface modification methods have been employed to illustrate the promise of Ln^{3+}-containing NIR-II nanoprobes in biodetection and bioimaging, the undesired side effects including toxicity and the long-term stability of Ln^{3+}-containing NIR-II nanoprobes should be eliminated prior to their use for *in vivo* bioapplications. To this end, more kinds of bioactive agents coating are expected to be further exploited. Moreover, fundamental studies of surface chemistry including surface interactions, surface charge, and surface functionality are still highly demanded for controllable surface engineering.

Last but not the least, most of the current NIR-II imaging techniques based on conventional single-modal NIR-II luminescent nanoprobes do not fully satisfy the clinical requirements. For NIR-II luminescent nanoprobes, it remains a challenge to provide sufficient anatomical information due to the limited tissue detection depth and poor quantification capability. To meet the demands of up-to-date biotechnology, the exploration of multimodal bioprobes by combining other emerging modalities (*e.g.*, magnetic resonance imaging, X-ray computed tomography imaging and photoacoustic imaging) with NIR-II luminescence of Ln^{3+}-containing nanoprobes is essential to accelerate their clinical translation. It should be noted that the NIR-II imaging studies associated with drug treatment have been rarely reported. The strategies for the construction of multimodal Ln^{3+}-containing NIR-II luminescent nanoprobes, which provide better data integration and validated results of each single-modal technique, will facilitate the precise therapeutic applications.

ACKNOWLEDGMENTS

This work was supported by the Science and Technology Cooperation Fund between Chinese and Australian Governments (No. 2017YFE0132300), the Strategic Priority Research Program of the Chinese Academy of Sciences (XDB20000000), the NSFC (No. 21975257, 21771185, 12074380, 11704380 and U1805252), the CAS/SAFEA International Partnership Program for Creative Research Teams, NSF of Fujian Province (No. 2019I0029).

AUTHOR CONTRIBUTIONS

Conceptualization, Y. J. Y., D. T. T., and X. Y. C.; Investigation, Y. J. Y., Y. Q. Z., and P. Z.; Writing–Original Draft, Y. J. Y. and D. T. T.; Writing–Review&Editing, Y. J. Y., D. T. T., Y. Q. Z., X. Y. C.; Supervision, X. Y. C and D. T. T.; Funding Acquisition, X. Y. C and D. T. T.

DECLARATION OF INTERESTS

The authors declare no conflict of interest.

REFERENCES

Antaris, A.L., Chen, H., Cheng, K., Sun, Y., Hong, G.S., Qu, C.R., Diao, S., Deng, Z.X., Hu, X.M., Zhang, B., et al. (2016). A small-molecule dye for NIR-II imaging. Nat. Mater. *15*, 235–242.

Chen, G.Y., Ohulchanskyy, T.Y., Liu, S., Law, W.C., Wu, F., Swihart, M.T., Agren, H., and Prasad, P.N. (2012). Core/shell $NaGdF_4$:Nd^{3+}/$NaGdF_4$ nanocrystals with efficient near-infrared to near-infrared downconversion photoluminescence for bioimaging applications. ACS Nano *6*, 2969–2977.

Cheng, X.W., Pan, Y., Yuan, Z., Wang, X.W., Su, W.H., Yin, L.S., Xie, X.J., and Huang, L. (2018). Er^{3+} sensitized photon upconversion nanocrystals. Adv. Funct. Mater. *28*, 1800208.

Dai, Y., Yang, D.P., Yu, D.P., Cao, C., Wang, Q.H., Xie, S.H., Shen, L., Feng, W., and Li, F.Y. (2017). Mussel-inspired polydopamine-coated lanthanide nanoparticles for NIR-II/CT dual imaging and photothermal therapy. ACS Appl. Mater. Inter. *9*, 26674–26683.

Diao, S., Blackburn, J.L., Hong, G.S., Antaris, A.L., Chang, J.L., Wu, J.Z., Zhang, B., Cheng, K., Kuo, C.J., and Dai, H.J. (2015). Fluorescence imaging in vivo at wavelengths beyond 1500 nm. Angew. Chem. Int. Ed. *54*, 14758–14762.

Dong, B.H., Li, C.Y., Chen, G.C., Zhang, Y.J., Zhang, Y., Deng, M.J., and Wang, Q.B. (2013). Facile synthesis of highly photoluminescent Ag_2Se quantum dots as a new fluorescent probe in the second near-infrared window for in vivo imaging. Chem. Mater. *25*, 2503–2509.

Dumont, M.F., Baligand, C., Li, Y., Knowles, E.S., Meisel, M.W., Walter, G.A., and Talham, D.R. (2012). DNA surface modified gadolinium phosphate nanoparticles as MRI contrast agents. Bioconjug. Chem. *23*, 951–957.

Escobedo, J.O., Rusin, O., Lim, S., and Strongin, R.M. (2010). NIR dyes for bioimaging applications. Curr. Opin. Chem. Biol. *14*, 64–70.

Fan, Y., Wang, P.Y., Lu, Y.Q., Wang, R., Zhou, L., Zheng, X.L., Li, X.M., Piper, J.A., and Zhang, F. (2018). Lifetime-engineered NIR-II nanoparticles unlock multiplexed in vivo imaging. Nat. Nanotechnol. *13*, 941–946.

Fan, Y., and Zhang, F. (2019). A new generation of NIR-II probes: lanthanide-based nanocrystals for bioimaging and biosensing. Adv. Opt. Mat. *7*, 1801417.

Gu, Y.Y., Guo, Z.Y., Yuan, W., Kong, M.Y., Liu, Y.L., Liu, Y.T., Gao, Y.L., Feng, W., Wang, F., Zhou, J.J., et al. (2019). High-sensitivity imaging of time-domain near-infrared light transducer. Nat. Photon. *13*, 580.

Hazra, C., Ullah, S., Correales, Y., Caetano, L., and Ribeiro, S. (2018). Enhanced NIR-I emission from water-dispersible NIR-II dye-sensitized core/active shell upconverting nanoparticles. J. Mater. Chem. C *6*, 4777–4785.

He, F., Yang, G., Yang, P., Yu, Y., Lv, R., Li, C., Dai, Y., Gai, S., and Lin, J. (2015). A new single 808 nm NIR light-induced imaging-guided multifunctional cancer therapy platform. Adv. Funct. Mater. *25*, 3966–3976.

He, S.Q., Chen, S., Li, D.F., Wu, Y.F., Zhang, X., Liu, J.F., Song, J., Liu, L.W., Qu, J.L., and Cheng, Z. (2019). High affinity to skeleton rare earth doped nanoparticles for near-infrared II imaging. Nano Lett. *19*, 2985–2992.

He, S.Q., Song, J., Qu, J.L., and Cheng, Z. (2018). Crucial breakthrough of second near-infrared biological window fluorophores: design and synthesis toward multimodal imaging and theranostics. Chem. Soc. Rev. *47*, 4258–4278.

Heffern, M.C., Matosziuk, L.M., and Meade, T.J. (2014). Lanthanide probes for bioresponsive imaging. Chem. Rev. *114*, 4496–4539.

Hong, G.S., Zou, Y.P., Antaris, A.L., Diao, S., Wu, D., Cheng, K., Zhang, X.D., Chen, C.X., Liu, B., He, Y.H., et al. (2014). Ultrafast fluorescence imaging in vivo with conjugated polymer fluorophores in the second near-infrared window. Nat. Commun. *5*, 4206.

Hu, J.Y., Ning, Y.Y., Meng, Y.S., Zhang, J., Wu, Z.Y., Gao, S., and Zhang, J.L. (2017). Highly near-IR emissive ytterbium(III) complexes with unprecedented quantum yields. Chem. Sci. *8*, 2702–2709.

Hu, Z.H., Chen, W.H., Tian, J., and Cheng, Z. (2020a). NIRF nanoprobes for cancer molecular imaging: approaching clinic. Trends Mol. Med. *26*, 469–482.

Hu, Z.H., Fang, C., Li, B., Zhang, Z.Y., Cao, C.G., Cai, M.S., Su, S., Sun, X.W., Shi, X.J., and Li, C. (2020b). First-in-human liver-tumour surgery guided by multispectral fluorescence imaging in the visible and near-infrared-I/II windows. Nat. Biomed. Eng. *4*, 259.

Huang, P., Tu, D., Zheng, W., Zhou, S., Chen, Z., and Chen, X. (2015). Inorganic lanthanide nanoprobes for background-free luminescent bioassays. Sci. China Mater. *58*, 156–177.

Huang, P., Zheng, W., Tu, D.T., Shang, X.Y., Zhang, M.R., Li, R.F., Xu, J., Liu, Y., and Chen, X.Y. (2019). Unraveling the electronic structures of neodymium in $LiLuF_4$ nanocrystals for ratiometric temperature sensing. Adv. Sci. *6*, 1802282.

Jin, G.Q., Ning, Y.Y., Geng, J.X., Jiang, Z.F., Wang, Y., and Zhang, J.L. (2020). Joining the journey to near infrared (NIR) imaging: the emerging role of lanthanides in the designing of molecular probes. Inorg. Chem. Front. *7*, 289–299.

Johnson, N.J.J., He, S., Diao, S., Chan, E.M., Dai, H.J., and Almutairi, A. (2017). Direct evidence for coupled surface and concentration quenching dynamics in lanthanide-doped nanocrystals. J. Am. Chem. Soc. *139*, 3275–3282.

Kantamneni, H., Zevon, M., Donzanti, M.J., Zhao, X.Y., Sheng, Y., Barkund, S.R., McCabe, L.H., Banach-Petrosky, W., Higgins, L.M., Ganesan, S., et al. (2017). Surveillance nanotechnology for multi-organ cancer metastases. Nat. Biomed. Eng. *1*, 993–1003.

Klik, M.A.J., Gregorkiewicz, T., Bradley, I.V., and Wells, J.P.R. (2002). Optically induced deexcitation of rare-earth ions in a semiconductor matrix. Phys. Rev. Lett. *89*, 227401.

Kodach, V.M., Kalkman, J., Faber, D.J., and van Leeuwen, T.G. (2010). Quantitative comparison of the OCT imaging depth at 1300 nm and 1600 nm. Biomed. Opt. Express *1*, 176–185.

Kong, Y.F., Chen, J., Fang, H.W., Heath, G., Wo, Y., Wang, W.L., Li, Y.X., Guo, Y., Evans, S.D., Chen, S.Y., et al. (2016). Highly fluorescent ribonuclease-A-encapsulated lead sulfide quantum dots for ultrasensitive fluorescence in vivo imaging in the second near-infrared window. Chem. Mater. *28*, 3041–3050.

Lei, X.L., Li, R.F., Tu, D.T., Shang, X.Y., Liu, Y., You, W.W., Sun, C.X., Zhang, F., and Chen, X.Y. (2018). Intense near-infrared-II luminescence from $NaCeF_4$:Er/Yb nanoprobes for in vitro bioassay and in vivo bioimaging. Chem. Sci. *9*, 4682–4688.

Li, D., He, S., Wu, Y., Liu, J., Liu, Q., Chang, B., Zhang, Q., Xiang, Z., Yuan, Y., Jian, C., et al. (2019a). Excretable lanthanide nanoparticle for biomedical imaging and surgical navigation in the second near-infrared window. Adv. Sci. *6*, 1902042.

Li, H., Hao, S., Yang, C., and Chen, G. (2017). Synthesis of multicolor core/shell $NaLuF_4$:Yb^{3+}/In^{3+}@CaF_2 upconversion nanocrystals. Nanomaterials *7*, 34.

Li, H., Wang, X., Li, X.L., Zeng, S.J., and Chen, G.Y. (2020a). Clearable shortwave-infrared-emitting $NaErF_4$ nanoparticles for noninvasive dynamic vascular imaging. Chem. Mater. *32*, 3365–3375.

Li, W.J., Zhan, P., De Clercq, E., Lou, H.X., and Liu, X.Y. (2013). Current drug research on PEGylation with small molecular agents. Prog. Polym. Sci. *38*, 421–444.

Li, X.L., Jiang, M.Y., Li, Y.B., Xue, Z.L., Zeng, S.J., and Liu, H.R. (2019b). 808 nm laser-triggered NIR-II emissive rare-earth nanoprobes for small tumor detection and blood vessel imaging. Mater. Sci. Eng. C Mater. Biol. Appl. *100*, 260–268.

Li, X.L., Jiang, M.Y., Zeng, S.J., and Liu, H.R. (2019c). Polydopamine coated multifunctional lanthanide theranostic agent for vascular malformation and tumor vessel imaging beyond 1500 nm and imaging-guided photothermal therapy. Theranostics *9*, 3866–3878.

Li, Z., Ding, X., Cong, H., Wang, S., Yu, B., and Shen, Y. (2020b). Recent advances on inorganic lanthanide-doped NIR-II fluorescence nanoprobes for bioapplication. J. Lumin. *228*, 117627.

Li, Z., Wu, J.J., Wang, Q.R., Liang, T., Ge, J., Wang, P.P., and Liu, Z.H. (2020c). A universal strategy to construct lanthanide-doped nanoparticles-based activable NIR-II luminescence probe for bioimaging. iScience *23*, 100962.

Liu, L., Wang, S.F., Zhao, B.Z., Pei, P., Fan, Y., Li, X.M., and Zhang, F. (2018). Er^{3+} sensitized 1530nm to 1180 nm second near-infrared window upconversion nanocrystals for *in vivo* biosensing. Angew. Chem. Int. Ed. *57*, 7518–7522.

Liu, Y.S., Luo, W.Q., Zhu, H.M., and Chen, X.Y. (2011). Optical spectroscopy of lanthanides doped in wide band-gap semiconductor nanocrystals. J. Lumin. *131*, 415–422.

Martín-Rodríguez, R., Geitenbeek, R., and Meijerink, A. (2013). Incorporation and luminescence of Yb^{3+} in CdSe nanocrystals. J. Am. Chem. Soc. *135*, 13668–13671.

Naczynski, D.J., Sun, C., Turkcan, S., Jenkins, C., Koh, A.L., Ikeda, D., Pratx, G., and Xing, L. (2015). X-ray-Induced shortwave infrared biomedical imaging using RareEarth nanoprobes. Nano Lett. *15*, 96–102.

Naczynski, D.J., Tan, M.C., Riman, R.E., and Moghe, P.V. (2014). Rare earth nanoprobes for functional biomolecular imaging and theranostics. J. Mater. Chem. B *2*, 2958–2973.

Naczynski, D.J., Tan, M.C., Zevon, M., Wall, B., Kohl, J., Kulesa, A., Chen, S., Roth, C.M., Riman, R.E., and Moghe, P.V. (2013). Rare-earth-doped biological composites as in vivo shortwave infrared reporters. Nat. Commun. *4*, 2199.

Ning, Y.Y., Zhu, M.L., and Zhang, J.L. (2019). Near-infrared (NIR) lanthanide molecular probes for bioimaging and biosensing. Coord. Chem. Rev. *399*, 213028.

Pan, G.C., Bai, X., Yang, D.W., Chen, X., Jing, P.T., Qu, S.N., Zhang, L.J., Zhou, D.L., Zhu, J.Y., Xu, W., et al. (2017). Doping lanthanide into perovskite nanocrystals: highly improved and expanded optical properties. Nano Lett. *17*, 8005–8011.

Peng, X.X., Zhu, X.F., and Zhang, J.L. (2020). Near infrared (NIR) imaging: exploring biologically relevant chemical space for lanthanide complexes. J. Inorg. Biochem. *209*, 111118.

Quintanilla, M., Zhang, Y., and Liz-Marzán, L.M. (2018). Subtissue plasmonic heating monitored with CaF_2:Nd^{3+}, Y^{3+} nanothermometers in the second biological window. Chem. Mater. *30*, 2819–2828.

Reineck, P., and Gibson, B.C. (2017). Near-infrared fluorescent nanomaterials for bioimaging and sensing. Adv. Opt. Mat. *5*, 1600446.

Semonin, O.E., Johnson, J.C., Luther, J.M., Midgett, A.G., Nozik, A.J., and Beard, M.C. (2010). Absolute photoluminescence quantum yields of IR-26 dye, PbS, and PbSe quantum dots. J. Phys. Chem. Lett. *1*, 2445–2450.

Shen, J., Chen, G.Y., Ohulchanskyy, T.Y., Kesseli, S.J., Buchholz, S., Li, Z.P., Prasad, P.N., and Han, G. (2013). Tunable near infrared to ultraviolet upconversion luminescence enhancement in (alpha-$NaYF_4$:Yb, Tm)/CaF_2 core/shell nanoparticles for in situ real-time recorded biocompatible photoactivation. Small *9*, 3213–3217.

Shen, Q., Wang, S.X., Yang, N.D., Zhang, C.W., Wu, Q., and Yu, C.M. (2020). Recent development of small -molecule organic fluorophores for multifunctional bioimaging in the second near -infrared window. J. Lumin. *225*, 117338.

Song, X.R., Li, S.H., Guo, H.H., You, W.W., Shang, X.Y., Li, R.F., Tu, D.T., Zheng, W., Chen, Z., Yang, H.H., et al. (2019). Graphene-oxide-modified lanthanide nanoprobes for tumor-targeted

visible/NIR-II luminescence imaging. Angew. Chem. Int. Ed. *58*, 18981–18986.

Stouwdam, J.W., and van Veggel, F. (2002). Near-infrared emission of redispersible Er^{3+}, Nd^{3+}, and Ho^{3+} doped LaF_3 nanoparticles. Nano Lett. *2*, 733–737.

Swabeck, J.K., Fischer, S., Bronstein, N.D., and Alivisatos, A.P. (2018). Broadband sensitization of lanthanide emission with indium phosphide quantum dots for visible to near-infrared downshifting. J. Am. Chem. Soc. *140*, 9120–9126.

Tan, M., del Rosal, B., Zhang, Y., Rodriguez, E., Hu, J., Zhou, Z., Fan, R., Ortgies, D., Fernandez, N., Chaves-Coira, I., et al. (2018). Rare-earth-doped fluoride nanoparticles with engineered long luminescence lifetime for time-gated in vivo optical imaging in the second biological window. Nanoscale *10*, 17771–17780.

Tan, M., Li, F., Cao, N., Li, H., Wang, X., Zhang, C., Jaque, D., and Chen, G. (2020). Accurate in vivo nanothermometry through NIR-II lanthanide luminescence lifetime. Small *2020*, 2004118.

Tang, S.Y., Sun, X.J., Lin, L., Sun, Y., and Liu, X.B. (2011). Monodisperse mesoporous silica nanoparticles: synthesis and application in biomaterials. Prog. Chem. *23*, 1973–1984.

Thimsen, E., Sadtler, B., and Berezin, M.Y. (2017). Shortwave-infrared (SWIR) emitters for biological imaging: a review of challenges and opportunities. Nanophotonics *6*, 1043–1054.

Tu, D.T., Liu, Y.S., Zhu, H.M., Li, R.F., Liu, L.Q., and Chen, X.Y. (2013). Breakdown of crystallographic site symmetry in lanthanide-doped $NaYF_4$ crystals. Angew. Chem. Int. Ed. *52*, 1128–1133.

Wang, D., Wang, D.P., Kuzmin, A., Pliss, A., Shao, W., Xia, J., Qu, J.L., and Prasad, P.N. (2018a). ICG-sensitized $NaYF_4$:Er nanostructure for theranostics. Adv. Opt. Mater. *6*, 1701142.

Wang, D., Wang, R., Liu, L., Qu, Y., Wang, G., and Li, Y. (2017a). Down-shifting luminescence of water soluble $NaYF_4$:Eu^{3+}@Ag core-shell nanocrystals for fluorescence turn-on detection of glucose. Sci. China Mater. *60*, 68–74.

Wang, P.Y., Fan, Y., Lu, L.F., Liu, L., Fan, L.L., Zhao, M.Y., Xie, Y., Xu, C.J., and Zhang, F. (2018b). NIR-II nanoprobes in-vivo assembly to improve image-guided surgery for metastatic ovarian cancer. Nat. Commun. *9*, 2898.

Wang, R., Li, X.M., Zhou, L., and Zhang, F. (2014). Epitaxial seeded growth of rare-earth nanocrystals with efficient 800 nm near-infrared to 1525 nm short-wavelength infrared downconversion photoluminescence for in vivo bioimaging. Angew. Chem. Int. Ed. *53*, 12086–12090.

Wang, X., Yakovliev, A., Ohulchanskyy, T.Y., Wu, L., Zeng, S.J., Han, X.J., Qu, J.L., and Chen, G.Y. (2018d). Efficient Erbium-Sensitized Core/Shell Nanocrystals for Short Wave Infrared Bioimaging. Adv. Opt. Mat. *6*, 1800690.

Wang, R., and Zhang, F. (2014). NIR luminescent nanomaterials for biomedical imaging. J. Mater. Chem. B *2*, 2422–2443.

Wang, R., and Zhang, F. (2016). Lanthanide-based near infrared nanomaterials for bioimaging. In Near Infrared Nanomaterials: Preparation, Bioimaging and Therapy Applications, F. Zhang, ed. (Royal Society of Chemistry), pp. 1–39.

Wang, R., Zhou, L., Wang, W.X., Li, X.M., and Zhang, F. (2017b). In vivo gastrointestinal drug-release monitoring through second near-infrared window fluorescent bioimaging with orally delivered microcarriers. Nat. Commun. *8*, 14702.

Wang, X.D., Shi, J.P., Li, P.H., Zheng, S.H., Sun, X., and Zhang, H.W. (2019). $LuPO_4$:Nd^{3+} nanophosphors for dual-mode deep tissue NIR-II luminescence/CT imaging. J. Lumin. *209*, 420–426.

Wang, Y.F., Liu, G.Y., Sun, L.D., Xiao, J.W., Zhou, J.C., and Yan, C.H. (2013). Nd^{3+}-Sensitized upconversion nanophosphors: efficient in vivo bioimaging probes with minimized heating effect. ACS Nano *7*, 7200–7206.

Wang, X., Hu, H.S., Zhang, H.L., Li, C.Y., An, B.L., and Dai, J.W. (2018c). Single ultrasmall Mn^{2+}-doped $NaNdF_4$ nanocrystals as multimodal nanoprobes for magnetic resonance and second near-infrared fluorescence imaging. Nano Res. *11*, 1069–1081.

Wang, Z.Y., Jiao, H., and Fu, Z.L. (2018e). Investigating the luminescence behaviors and temperature sensing properties of rare-earth-doped $Ba_2In_2O_5$ phosphors. Inorg. Chem. *57*, 8841–8849.

Welsher, K., Liu, Z., Sherlock, S.P., Robinson, J.T., Chen, Z., Daranciang, D., and Dai, H.J. (2009). A route to brightly fluorescent carbon nanotubes for near-infrared imaging in mice. Nat. Nanotechnol. *4*, 773–780.

Xia, A., Chen, M., Gao, Y., Wu, D.M., Feng, W., and Li, F.Y. (2012). Gd^{3+} complex-modified $NaLuF_4$-based upconversion nanophosphors for trimodality imaging of NIR-to-NIR upconversion luminescence, X-Ray computed tomography and magnetic resonance. Biomaterials *33*, 5394–5405.

Xiao, Q.B., Zhu, H.M., Tu, D.T., Ma, E., and Chen, X.Y. (2013). Near-Infrared-to-Near-Infrared downshifting and near-infrared-to-visible upconverting luminescence of Er^{3+}-doped In2O3 Nanocrystals. J. Phys. Chem. C *117*, 10834–10841.

Xu, J.T., Gulzar, A., Yang, P.P., Bi, H.T., Yang, D., Gai, S.L., He, F., Lin, J., Xing, B.G., and Jin, D.Y. (2019). Recent advances in near-infrared emitting lanthanide-doped nanoconstructs: mechanism, design and application for bioimaging. Coordin. Chem. Rev. *381*, 104–134.

Xu, S.Y., Cui, J.B., and Wang, L.Y. (2016). Recent developments of low-toxicity NIR II quantum dots for sensing and bioimaging. Trends. Anal. Chem. *80*, 149–155.

Xue, Z.L., Zeng, S.J., and Hao, J.H. (2018). Non-invasive through-skull brain vascular imaging and small tumor diagnosis based on NIR-II emissive lanthanide nanoprobes beyond 1500 nm. Biomaterials *171*, 153–163.

You, W.W., Tu, D.T., Zheng, W., Shang, X.Y., Song, X.R., Zhou, S.Y., Liu, Y., Li, R.F., and Chen, X.Y. (2018). Large-scale synthesis of uniform lanthanide-doped $NaREF_4$ upconversion/downshifting nanoprobes for bioapplications. Nanoscale *10*, 11477–11484.

Yu, S.H., Tu, D.T., Lian, W., Xu, J., and Chen, X.Y. (2019). Lanthanide-doped near-infrared II luminescent nanoprobes for bioapplications. Sci. China Mater. *62*, 1071–1086.

Yu, X.F., Chen, L.D., Li, M., Xie, M.Y., Zhou, L., Li, Y., and Wang, Q.Q. (2008). Highly efficient fluorescence of NdF_3/SiO_2 core/shell nanoparticles and the applications for in vivo NIR detection. Adv. Mater. *20*, 4118–4123.

Yu, Z., Shi, J.C., Li, J.L., Li, P.H., and Zhang, H.W. (2018). Luminescence enhancement of CaF_2:Nd^{3+} nanoparticles in the second near-infrared window for in vivo imaging through Y^{3+} doping. J. Mater. Chem. B *6*, 1238–1243.

Yu, Z.F., Eich, C., and Cruz, L.J. (2020). Recent advances in rare-earth-doped nanoparticles for NIR-II imaging and cancer theranostics. Front. Chem. *8*, 496.

Zhang, H.X., Chen, Z.H., Liu, X., and Zhang, F. (2020a). A mini-review on recent progress of new sensitizers for luminescence of lanthanide doped nanomaterials. Nano Res. *13*, 1795–1809.

Zhang, H.X., Fan, Y., Pei, P., Sun, C.X., Lu, L.F., and Zhang, F. (2019a). Tm^{3+}-Sensitized NIR-II fluorescent nanocrystals for in vivo information storage and decoding. Angew. Chem. Int. Ed. *58*, 10153–10157.

Zhang, M.R., Zheng, W., Liu, Y., Huang, P., Gong, Z.L., Wei, J.J., Gao, Y., Zhou, S.Y., Li, X.J., and Chen, X.Y. (2019b). A new class of blue-LED-excitable NIR-II luminescent nanoprobes based on lanthanide-doped CaS nanoparticles. Angew. Chem. Int. Ed. *58*, 9556–9560.

Zhang, T.R., Ge, J.P., Hu, Y.X., and Yin, Y.D. (2007). A general approach for transferring hydrophobic nanocrystals into water. Nano Lett. *7*, 3203–3207.

Zhang, W., Xu, C., Yin, G.-Q., Zhang, X.-E., Wang, Q., and Li, F. (2017). Encapsulation of inorganic nanomaterials inside virus-based nanoparticles for bioimaging. Nanotheranostics *1*, 358–368.

Zhang, X., He, S.Q., Ding, B.B., Qu, C.R., Zhang, Q., Chen, H., Sun, Y., Fang, H.Y., Long, Y., Zhang, R.P., et al. (2020b). Cancer cell membrane-coated rare earth doped nanoparticles for tumor surgery navigation in NIR-II imaging window. Chem. Eng. J. *385*, 123959.

Zhang, X.W., Zhao, Z., Zhang, X., Cordes, D.B., Weeks, B., Qiu, B.S., Madanan, K., Sardar, D., and Chaudhuri, J. (2015). Magnetic and optical properties of $NaGdF_4$:Nd^{3+}, Yb^{3+}, Tm^{3+} nanocrystals with upconversion/downconversion luminescence from visible to the near-infrared second window. Nano Res. *8*, 636–648.

Zhang, Y.X., Huang, P., Wang, D., Chen, J.C., Liu, W.Z., Hu, P., Huang, M.D., Chen, X.Y., and Chen, Z. (2018). Near-infrared-triggered antibacterial and antifungal photodynamic therapy based on lanthanide-doped upconversion nanoparticles. Nanoscale *10*, 15485–15495.

Zhao, M.Y., Li, B.H., Wu, Y.F., He, H.S., Zhu, X.Y., Zhang, H.X., Dou, C.R., Feng, L.S., Fan, Y., and Zhang, F. (2020). A tumor-microenvironment-responsive lanthanide-cyanine FRET sensor for NIR-II luminescence-lifetime in situ imaging of hepatocellular carcinoma. Adv. Mater. *32*, 2001172.

Zhao, M.Y., Wang, R., Li, B.H., Fan, Y., Wu, Y.F., Zhu, X.Y., and Zhang, F. (2019). Precise InVivo inflammation imaging using InSitu responsive cross-linking of glutathione-modified ultra-small NIR-II lanthanide nanoparticles. Angew. Chem. Int. Ed. *58*, 2050–2054.

Zheng, W., Huang, P., Tu, D.T., Ma, E., Zhu, H.M., and Chen, X.Y. (2015). Lanthanide-doped upconversion nano-bioprobes: electronic structures, optical properties, and biodetection. Chem. Soc. Rev. *44*, 1379–1415.

Zhong, Y.T., and Dai, H.J. (2020). A mini-review on rare-earth down-conversion nanoparticles for NIR-II imaging of biological systems. Nano Res. *13*, 1281–1294.

Zhong, Y.T., Ma, Z.R., Wang, F.F., Wang, X., Yang, Y.J., Liu, Y.L., Zhao, X., Li, J.C., Du, H.T., Zhang, M.X., et al. (2019). In vivo molecular imaging for immunotherapy using ultra-bright near-infrared-IIb rare-earth nanoparticles. Nat. Biotechnol. *37*, 1322–1331.

Zhong, Y.T., Ma, Z.R., Zhu, S.J., Yue, J.Y., Zhang, M.X., Antaris, A.L., Yuan, J., Cui, R., Wan, H., Zhou, Y., et al. (2017). Boosting the down-shifting luminescence of rare-earth nanocrystals for biological imaging beyond 1500 nm. Nat. Commun. *8*, 737.

Zhou, J.J., Shirahata, N., Sun, H.T., Ghosh, B., Ogawara, M., Teng, Y., Zhou, S.F., Chu, R.G.S., Fujii, M.R., and Qiu, J.R. (2013). Efficient dual-modal NIR-to-NIR emission of rare earth ions Co-doped nanocrystals for biological fluorescence imaging. J. Phys. Chem. Lett. *4*, 402–408.

Zhu, Y.S., Pan, G.C., Shao, L., Yang, G., Xu, X.M., Zhao, J., and Mao, Y.L. (2020). Effective infrared emission of erbium ions doped inorganic lead halide perovskite quantum dots by sensitization of ytterbium ions. J. Alloys Compd. *835*, 155390.

Zou, W.Q., Visser, C., Maduro, J.A., Pshenichnikov, M.S., and Hummelen, J.C. (2012). Broadband dye-sensitized upconversion of near-infrared light. Nat. Photon. *6*, 560–564.